AGU ADVANCING EARTH AND SPACE SCIENCE

Water Resources Research

RESEARCH ARTICLE
10.1029/2021WR030912

On the Role of Density-Driven Dissolution of CO_2 in Phreatic Karst Systems

H. Class[1], P. Bürkle[1], T. Sauerborn[1], O. Trötschler[1], B. Strauch[2], and M. Zimmer[2]

[1]Institute for Modelling Hydraulic and Environmental Systems, University of Stuttgart, Stuttgart, Germany, [2]GFZ German Research Centre for Geosciences, Potsdam, Germany

Key Points:

- Density-driven CO_2 dissolution is a process that deserves more attention in karstification theories and beyond
- Fluctuating CO_2 partial pressures in the vadose zone can enhance dissolution of CO_2 in phreatic karst water
- Generic scenarios are used to demonstrate how density-driven dissolution can contribute to replenishing CO_2 in karst water

Correspondence to:

H. Class,
holger.class@iws.uni-stuttgart.de

Citation:

Class, H., Bürkle, P., Sauerborn, T., Trötschler, O., Strauch, B., & Zimmer, M. (2021). On the role of density-driven dissolution of CO_2 in phreatic karst systems. *Water Resources Research*, *57*, e2021WR030912. https://doi.org/10.1029/2021WR030912

Received 28 JUL 2021
Accepted 2 DEC 2021

Author Contributions:

Conceptualization: H. Class, P. Bürkle, O. Trötschler
Funding acquisition: H. Class
Investigation: P. Bürkle, T. Sauerborn, B. Strauch, M. Zimmer
Methodology: H. Class, B. Strauch, M. Zimmer
Project Administration: H. Class
Software: H. Class
Supervision: H. Class
Writing – original draft: H. Class, P. Bürkle, T. Sauerborn, O. Trötschler, B. Strauch, M. Zimmer
Writing – review & editing: H. Class

Abstract Density-driven dissolution of carbon dioxide in water is a well-known and much described mechanism in geological sequestration of this greenhouse gas. It is remarkable that such enhanced dissolution does not receive attention in karst hydrology and speleology. Models and hypotheses on karst development are complex and consider many different processes. We focus here on the influence of CO_2 partial gas pressures at the interface between atmosphere and karst water on the dynamics of dissolved CO_2 concentrations below the water table. Seasonal variations of microbial soil activity and root respiration or barometric-pressure changes cause fluctuations in CO_2 partial pressures. Dependent on the existence and strength of a karst-water background flow, fingering regimes might be triggered causing enhanced dissolution of CO_2. This allows replenishment of CO_2, and, thus, dissolutional power even deep in the water body without the need for percolating water to transport dissolved CO_2. We present and discuss simplified and generic experimental and computational scenarios to strengthen our claim, and we try to give answers to: how much? and under which circumstances? The applied numerical model solves the Navier-Stokes equation with water density dependent on CO_2 concentration and temperature. We show that calculated CO_2 mass fluxes into the water bodies are dependent on the ratio of Péclet to Rayleigh numbers (Pe/Ra) and show a local minimum around Pe/Ra = 1, i.e. when natural and forced convection are about equal. Concluding, we claim that there is sufficient reason to consider density-driven dissolution as a process of relevance in karstification if circumstances are given.

Plain Language Summary Karst systems form in rocks, such as limestones, that are soluble in the presence of water charged with carbonic acid. The carbon dioxide (CO_2) can take different pathways to replenish dissolutional power in karst water. This study discusses a pathway that did not receive much attention yet. The density of water increases when CO_2 dissolves, and, when dissolution occurs at the water table, instabilities may be induced. This can trigger fingering-like flow and enhance the rate of dissolution at the water table. The phenomenon is well-known as a major trapping mechanism for CO_2 injected into geological formations for mitigating greenhouse-gas emissions. The more so is it remarkable that the same phenomenon is not discussed in karst hydrology and speleology. Of course, the different conditions of concentrations, pressures, and temperatures require attention. For realistic conditions, we demonstrate experimentally and by numerical simulations that density-induced transport of CO_2 is significant. The lab experiment used a 6 m long vertical column and imitates an analog to a cave lake. We can see that within a few months time, significant amounts of CO_2 can be dissolved at karst-typical elevated gaseous CO_2 concentrations. The influence of natural ground-/karst water background flow is addressed by numerical simulations.

1. Introduction

Karst systems are found in many regions around the world. In the order of 10% of the continental surface is karst (Ford & Williams, 2007; Mangin, 1975). Karst is incredibly complex and manifold, and the processes that dominate karstification strongly depend on the hydrological and geomorphological properties of the karstic systems, which are subject to constant change while karstification is ongoing. Essentially, karstification happens in soluble rocks in contact with water, typically at the earth's surface or close to it. Karst research has evident relations to the disciplines and sub-disciplines of hydrology, geology, speleology, geomorphology, hydrogeology, etc. Karstic rocks are typically carbonate rocks made of Calcium and Magnesium minerals, where limestone ($CaCO_3$) and dolomite ($CaMg[CO_3]_2$) are the most important subtypes. During karstification, these rocks are eroded mechanically, and, more importantly, corroded chemically. The corrosion of calcite and dolomite is driven by the availability of dissolved CO_2 in the water.

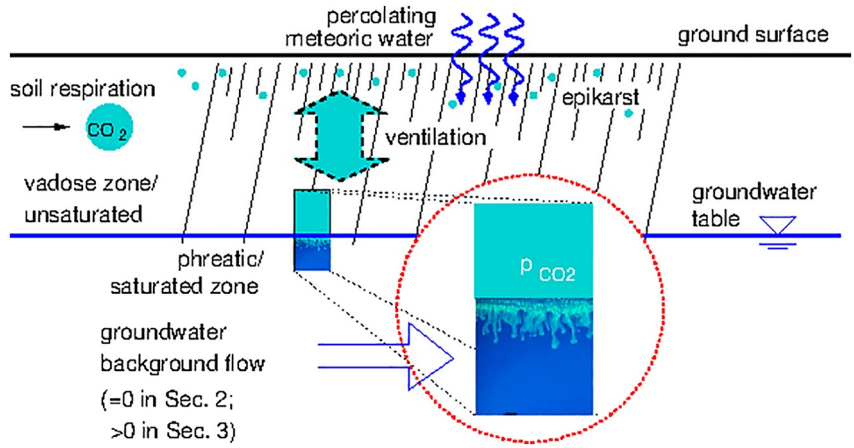

Figure 1. Schematic, strongly simplified setup to illustrate the focus of this study in karst context: in karst features at the water table we study the influence of fluctuating CO_2 partial pressures (p_{CO2}) in the air on dissolution of CO_2 into water bodies. We assume here that water bodies are either stagnant (as in Section 2) or exposed to small groundwater background flow (as in Section 3). In these cases, we focus on density-driven dissolution that leads to fingering as illustrated in the figure. We further assume that we have situations where flow in karst conduits is either absent or of no influence on the study area.

What is the origin of the CO_2 in karst systems and what are its migration pathways into karst water? Textbooks on karst research and a multitude of papers generally agree that CO_2 is produced and accumulated by seasonally fluctuating biological activity and root respiration in the vadose zone (Bonacci, 1987; Dreybrodt, 1988; Ford & Williams, 2007; Klimchouk et al., 2000; Stevanovic, 2015; White, 2018). The vadose zone is also denoted as the unsaturated zone, while karst literature often refers to epikarst as the subcutaneous vadose layer close to the ground surface, see also Figure 1. There, the CO_2 is dissolved by percolating meteoric water, and a hydraulic gradient is then required to transport water through the rock, where the aggressiveness of the CO_2-enriched water has a potential to dissolve carbonate. Flow and transport are crucially important, since the dissolved Ca^{2+} and carbonate ions will affect the reaction kinetics and the dissolution reaction will level out if the reaction products are not transported away. While we do not discuss hypogenic karst systems here - where solutional aggressiveness originates from sources in the depth - , it is generally accepted that in epigenic systems, the CO_2 has its origin in the epikarst above the karst-water table and requires downward transport due to percolating meteoric water or ventilation (Figure 1) to corrode carbonate rocks (e.g., Audra & Palmer, 2011; Bakalowicz, 2005; Houillon et al., 2020; Kaufmann et al., 2014; Klimchouk et al., 2000; Riechelmann et al., 2019; Spötl et al., 2016).

Consequently, more corrosion occurs at or close to the surface rather than deep inside the rock. An approach to explain the corrosion observed also deep inside employs mixing corrosion (or mixing dissolution) (Bögli, 1980). Two water flows, which are each in a different state of calco-carbonic equilibrium, always form a calcite-aggressive solution when they mix in joints. Another approach explains dissolution of calcite deep inside the rock with non-linear dissolution kinetics that allow for the water to keep some remaining dissolutional power while penetrating deep into the rock (e.g., Dreybrodt, 2004; Ford & Ewers, 1978; Gabrovšek & Dreybrodt, 2000; Kaufmann et al., 2014).

This study aims at supporting the claim that there is an additional process that can replenish CO_2 in epiphreatic karst water: density-driven dissolution of CO_2. This is a well-known process in geological storage of CO_2 and, denoted also as solubility trapping, acknowledged as a storage mechanism of major importance for safe long-term storage of this greenhouse gas in deep geological reservoirs (IPCC, 2005). The conditions there are obviously strongly different from conditions in rather shallow karst systems. In geologic reservoirs, CO_2 is typically in a supercritical state and its density is about half of the ambient brine's density. Thus, the CO_2 will first of all accumulate in a stratum underneath a caprock on top of the brine. Over time, CO_2 dissolves in the brine and increases the brine's density (e.g., Garcia, 2001). The layering may become instable and trigger a fingering process, eventually resulting in an enhanced dissolution and an effective vertical downward transport of CO_2. Solubility trapping has already been discussed in early publications in the field of CO_2 geological storage (e.g., Lindeberg & Wessel-Berg, 1997; Weir et al., 1996).

A phenomenological and mathematical description was given by Bénard (1901) and Lord Rayleigh (1916) for convective cells forming due to density differences induced by a fluid of lower temperature resting upon a fluid of higher temperature. The dimensionless Rayleigh number, Ra, is commonly employed to characterize this vertically oriented instability. Ra can be interpreted as the ratio of a characteristic diffusion time to a characteristic convection time. High Ra characterizes conditions favorable for convection, while diffusion is dominant in low Ra regimes. Related to CO_2 geological storage, (in-)stability analyses are discussed by many authors (e.g., Emami-Meybodi et al., 2015; Ennis-King & Paterson, 2003a, 2003b; Hassanzadeh et al., 2006, 2005, 2007; Riaz et al., 2006). High-resolution numerical studies on Darcy-type models for porous media also show that numerical modelling requires very small discretization length to resolve onset time and fingering patterns correctly (Pau et al., 2010; Riaz et al., 2006). Thus, grid-converged results on large spatial reservoir scales are practically infeasible. Pragmatic approaches avoid the resolution of the fingers and employ effective rates, dependent on permeability, viscosity, and density difference as a function of CO_2 concentration and brine salinity (Green & Ennis-King, 2018; Pau et al., 2010).

Density-driven CO_2 dissolution in karst systems finds strongly different conditions than in deep geological storage. CO_2 concentrations and partial pressures in the gaseous phase are much smaller. Consequently, also density differences that may trigger instability are smaller. On the other hand, the resistance to convective fingering in karst features like permeable fissures or open water bodies in cavities is less than in deep reservoirs.

Erfani et al. (2021) show that CO_2 density-driven flow in carbonate aquifers should not be viewed as an isolated processes but rather strongly coupled to geochemical processes that have significant impact on the convection processes. This holds a fortiori in karst aquifers and karstification where the coupling of flow with reaction drives the genesis and growth of conduits or caves on even longer time scales. Subsurface water can contain many different dissolved components, and water chemistry can become complex in its details. Keeping things as simple as possible, our interest is on the calco-carbonic system, and for this particular study we narrow the focus on CO_2 dissolving in water. While the majority of the CO_2 remains physically dissolved as CO_2 molecules, a small part of it forms with H_2O carbonic acid (H_2CO_3) which can dissociate into bicarbonate (HCO_3^-) and carbonate (CO_3^{2-}) by splitting off H^+. While the latter affect the pH value, responsible for solutional aggressiveness, the dissolved CO_2, H_2CO_3, HCO_3^-, and CO_3^{2-}, often summarized as total inorganic carbon (TIC) have impact on the water density. As in Erfani et al. (2021), the effect of dissolved ions on water density is aggravated also in karst systems, when for example, Ca^{++} ions are considered and vertically oriented fingering regimes are likely to receive further stimulation close to reactive carbonate surfaces.

In the following, we review karst-related literature and elaborate on different aspects in order to highlight where we believe that density-driven dissolution can contribute to closing knowledge-gaps or can provide better process-related explanations.

1. Open and closed systems need to be distinguished for interpreting cation concentrations in karst water. Open systems allow for an equilibrium between solid (carbonates), liquid water, and gas to establish over time, while in a closed system with no replenishment of CO_2, the final steady state is an equilibrium between the dissolved species dependent on their initial amounts. Atkinson (1977) suggests accordingly, that higher carbonate hardness of water, as a measure for the aqueous concentrations of cations, indicates a tendency toward an open system. Hardness is higher in open systems, since CO_2 availability is not the limiting factor. Atkinson (1977) further relates fluctuations and mean values of CO_2 soil concentrations with spring waters, which often show corresponding oscillations in $p_{CO_2,eq}$, the calculated partial pressures in assumed equilibrium. Larger groundwater bodies may dampen this in spring waters, where the $p_{CO_2,eq}$ is rather constant. Atkinson (1977), Figure 4, compares the detected hardness at springs with hardness of soil water and potential hardness according to the above-mentioned equilibrium in an open system. The detected hardness in spring water is much higher than the hardness of soil water. The potential hardness of soil water approaches the detected hardness, in summer months even exceeds it. Interestingly, and important for our case, the author concludes that the discrepancy must be made from another source of CO_2 in the air of the zone where water percolates. Our reasoning is, however, that this might well be the case, but we don't necessarily need to have the percolating water in contact with these high air concentrations. It can be sufficient or even be more effective to have these high CO_2 partial pressures at the karst water table where they trigger density-induced dissolution.
2. Hydraulic conditions and controls of epigenic speleogenesis are manifold and often complex. Audra and Palmer (2011) write on controls of epigenic caves, they discuss the different hydrologic zones in karst and

highlight the importance of the epiphreatic zone, where water-table fluctuations take place. Not all epiphreatic water may be connected, and local ponding due to local geologic features might occur. In the early history of a cave, water circulation is rather very small, since no good networks exist yet; there is low permeability, and water is nearly saturated with dissolved calcite. Later on, under hydraulic gradients, larger fluxes, even turbulence may occur. One may object, what if we have intermittent regimes, with periods where no or only very small hydraulic gradients exist? In such cases, density-driven dissolution may make a difference. Audra and Palmer (2011) further give an interesting review of earlier and current conceptual ideas which do not necessarily exclude each other, since nature is enormously manifold, and there might be many mechanisms adding to the overall picture.

3. Current theories point at the importance of water circulation as a control for the development of karst. Dreybrodt (1988) explains this in detail in his textbook. A free surface of the karst water, and, thus, an interface between the vadose zone and the saturated zone exists only at a later stage of karstification, when fissures or conduits have already developed. According to Dreybrodt (1988), karstification starts when a hydraulic gradient is acting in an interconnected system of primary, micro-size fissures of several 10 μ, upon which chemically aggressive groundwater dissolves the rock along these flow paths. This process is self-enhancing, since resistance to flow is reduced with increasing channel dimensions. Similar reasoning is found, for example, in Mangin (1975); Mohammadi et al. (2007); Ford and Ewers (1978). Circulation facilitates corrosion and vice versa; without circulation corrosion quickly stops. But what if water is not flowing? Or circulating only intermittently, or only at very small velocities? Is the reaction system then approaching a state of equilibrium? If CO_2 can sink into water bodies and replenish by enhanced dissolution, the process of karstification could go on without percolating water, and it may be sufficient that the reaction products are transported away intermittently. This might contribute to discussions on the role of mixing corrosion, which was described, for example, by Bögli (1980), and which was questioned and put into perspective by Gabrovšek and Dreybrodt (2000) and Dreybrodt (2004) using non-linear dissolution models while still requiring percolating water in fissures or bedding planes. Consequently, density-driven dissolution during periods without or only small water percolation is yet another explanation for replenishment of CO_2.
4. Fluctuations in vadose CO_2 gas concentrations are recognized as an important driving force for enhancing carbonate dissolution. Gulley et al. (2014) show that CO_2 in the vadose gas, and in particular fluctuations in the partial pressure of CO_2 due to seasonal accumulation, can drive dissolution of carbonates more efficiently than mixing corrosion can explain, which is in fact very close to our conceptual idea. Still, they do not mention density-driven dissolution, but simply assume that dissolved CO_2 is evenly distributed throughout the upper 0.5 m of groundwater. More detail on CO_2 distribution is reported from a multi-year measurement campaign by Houillon et al. (2020), who provided weather data (atmospheric pressure, temperature, rain events), p_{CO_2} in soil, bicarbonate concentration measured in drip water, and $p_{CO_2,eq}$ in (assumed) equilibrium determined with a CO_2-SIc relationship (Peyraube et al., 2015). Soil $p_{CO_2,eq}$, as expected, showed seasonal variation with strong biogenic production in spring and lower production during autumn and winter. They also measured soil CO_2 efflux, which was, again as expected, higher in summer than in winter. But interestingly, it varied strongly with soil moisture. Dry soil correlates with high CO_2 efflux, wet soil (after rain events) with low efflux. Soil moisture and temperature clearly act as an important control for vertical transport of CO_2 in the vadose zone. Furthermore, it is known that in places with vertical upward ventilation during cold periods fresh air is transported into the cave system and dilutes high CO_2 concentration, while downward transport in warm periods enriches the cave's air with CO_2 (Riechelmann et al., 2019). Kukuljan et al. (2021) conducted a comprehensive study on CO_2 dynamics in a karst system in Slovenia related to microclimatic observations and showed that this typical behavior due to the so-called chimney effect can be superimposed by wind gusts. This can lead to extremely complex ventilation patterns that constantly enforce dilution and enrichment of cave air. Thus, seasonally fluctuating CO_2 concentrations at the epiphreatic interface are sufficiently well understood to claim that, where background flow is absent or small, dissolution of CO_2 generates corresponding water-density gradients as required for triggering density-driven dissolution.
5. Studies on carbon isotopes may give hints at favorable conditions for density-driven dissolution of CO_2, although the reasoning below is a bit speculative. The fractionation between the stable carbon isotopes ^{13}C and ^{12}C is often employed to interpret different climatic controls on conditions in karstification. Plants prefer the lighter isotope and discriminate against ^{13}C (Werth & Kuzyakov, 2010). Therefore, $\delta^{13}C$ data, as found, for example, in speleothems (Fohlmeister et al., 2020; Riechelmann et al., 2019; White, 2018) or in karstic spring waters (Lee et al., 2021), can be used to conclude on effects from different vegetation, soil moisture,

temperature, or soil respiration. CO_2 concentrations in karst systems typically show significant contributions from vegetation and soil respiration, while the processes affecting respiration and plant growth are extremely complex, also with inhibitory effects when CO_2 concentrations are high (Ben-Noah & Friedman, 2018). Fohlmeister et al. (2020) found in speleothems that high $\delta^{13}C$ values correlate with caves in which ventilation is strong. Ventilation facilitates the mixing of atmospheric CO_2 into the soil gas and, thus, increases $\delta^{13}C$. We discussed above that ventilation affects the partial pressure of CO_2 as required for triggering density-driven dissolution. The study of Lee et al. (2021) reports extreme gradients of CO_2 found in karstic springs, where the authors also analyze ^{13}C. They were surprised to find strong spatial variability in dissolved CO_2 concentrations and in their $\delta^{13}C$, although all sample sites were in the same region (same climate, same geology). They assume that at sites with relatively high ^{13}C contents, it might be explained by more intense leaching of carbonate rocks (with higher $\delta^{13}C$) due to longer residence time of the water in the system. If however, now being speculative, this site was a case where conditions for density-driven dissolution were more favorable than in others, the postulated longer residence time might not necessarily be required for explaining the observation.

6. We conclude this brief literature review with Ma et al. (2014) and Serrano-Ortiz et al. (2010), who speculate about large subterranean depots for CO_2 in order to contribute to explaining an apparent imbalance between the amounts of CO_2 released from anthropogenic activities and documented terrestrial or oceanic sinks. They use expressions like 'hidden flows' or 'downward CO_2 fluxes which seem to have nowhere to go' and assume that groundwater acts as a major sink, although not providing details on mechanisms. We consider it possible that density-driven dissolution can be a contribution to this phenomenon.

In summary, we are not aware of literature discussing density-driven CO_2 dissolution in karstification, and we suggest that investigations on its potential significance should be structured along the following research questions:

1. What do we know about CO_2 dynamics in water bodies exposed to fluctuating CO_2 partial pressures at the water table? Can we measure it? And do we have numerical models that are capable of describing these processes? See also in Class et al. (2020)
2. What are the conditions for density-driven dissolution of CO_2 to occur, such that small density differences are sufficient to trigger instabilities?
3. Can we estimate density-driven CO_2 dissolution rates, for example, in phreatic caves?
4. Is density-driven CO_2 dissolution relevant for karst hydrology, geomorphology, or speleology?

In Figure 1, we illustrate in a very schematic outline our simplified, generic settings, which we use later on to elaborate on the formulated questions. Seasonal soil and root respiration produce CO_2, which is transported into deeper regions dissolved in water or as gas by ventilation, where partial gas pressures of CO_2 at the interface to the phreatic zone fluctuate accordingly. In the simplest case, groundwater background flow, i.e. forced horizontal advection that affects the vertically oriented fingering, is not existing. This sets the stage for Section 2, which investigates CO_2 dissolution into stagnant water in a 6 m tall laboratory column. Note that we also introduce a novel measurement setup for CO_2 concentrations in the water body. Section 3 presents exemplary scenarios with small groundwater background flow, which are aimed at demonstrating the influence of forced versus natural convection on the occurrence of density-driven dissolution and its relevance for the transfer of CO_2 from the gas phase into water bodies. Section 4 concludes with a discussion and an outlook, where we evaluate the significance of our findings toward answering the four research questions formulated above.

2. Stagnant Water Column Exposed to Elevated CO_2 Partial Pressures

We filled a laboratory column with tapwater and exposed it to an elevated gaseous CO_2 concentration, roughly 50 times the current atmospheric concentration, thus imitating cave-air conditions. After stripping the water with ambient air, it was initially in equilibrium with atmospheric conditions. Certainly not likely to happen exactly that way in a cave, this setup imitates the case of a cave lake, which quickly received fresh water, and is then exposed to CO_2-rich cave air conditions. Then, we measured the concentration of dissolved CO_2 over a time period of 60 days in two different depths in the column. The measured values can be compared to results of numerical simulations, thus allowing for a more substantiated discussion of related uncertainties and the relevance of the conclusions we can draw from this study.

Table 1
Water Parameters Before and After the Experiment, Obtained From Water Samples After Titration and Determination of TC and TOC. (Institute for Sanitary Engineering, Water Quality and Solid Waste Management, Personal Communication)

	Before	After	
pH	8.16	7.40	
p-value	0.046	0.570	mMol/l
m-value	2.65	2.85	mMol/l
TC	33.9	35.9	mg/l
TOC	2.07	1.53	mg/l
TC - TOC	30.9	34.9	mg/l

2.1. Experiment: Materials and Methods

With the design of the setup, we aimed (a) at providing well-controlled conditions, (b) at a cooling of the water to subsurface-like, close-to-constant temperatures, and (c) at defining as possible karst-representative CO_2 concentrations in the gas. Therefore, a 6 m long HDPE column (PE 100 SDR 11) with an outer diameter of 0.25 m (OD 250 × 22.7 mm wall thickness, thermal conductivity 0.38 W/(mK)) was filled with tapwater (Bodenseewasserversorgung, Stuttgart) and stripped with ambient air to initialize a CO_2-concentration in the water in equilibrium to ≈ 400 ppm gaseous concentration. Before the influx of CO_2 was started as well as after the experiment, water samples were taken and analyzed (Table 1).

Aiming at creating a cave-like atmosphere, we chose to define a target value of $x_{CO_2} = 20,000$ ppm ± 5, 000 ppm atmospheric CO_2-concentration above the water table at the top of the column, which was sealed from the ambient atmosphere with a 0.35 m long cylindrical head space. The head space serves as a lid with two chambers separated by a skimming wall to enforce mixing of the gas in the entire air chamber and to avoid a shortcut of the circulating CO_2-enriched air, see Figure 2. At the top of one of the chambers, CO_2 was added at times using a 100 l TEDLAR®-PVF bag filled with CO_2 (99.8% purity, atmospheric pressure), while the gas was pumped out from the top of the other chamber. After feeding the CO_2, a small flow of ≈5 l/min, using an air-membrane pump (KNF N86 KTE), was maintained in the head space across the skimming wall. The process is illustrated in Figure 2.

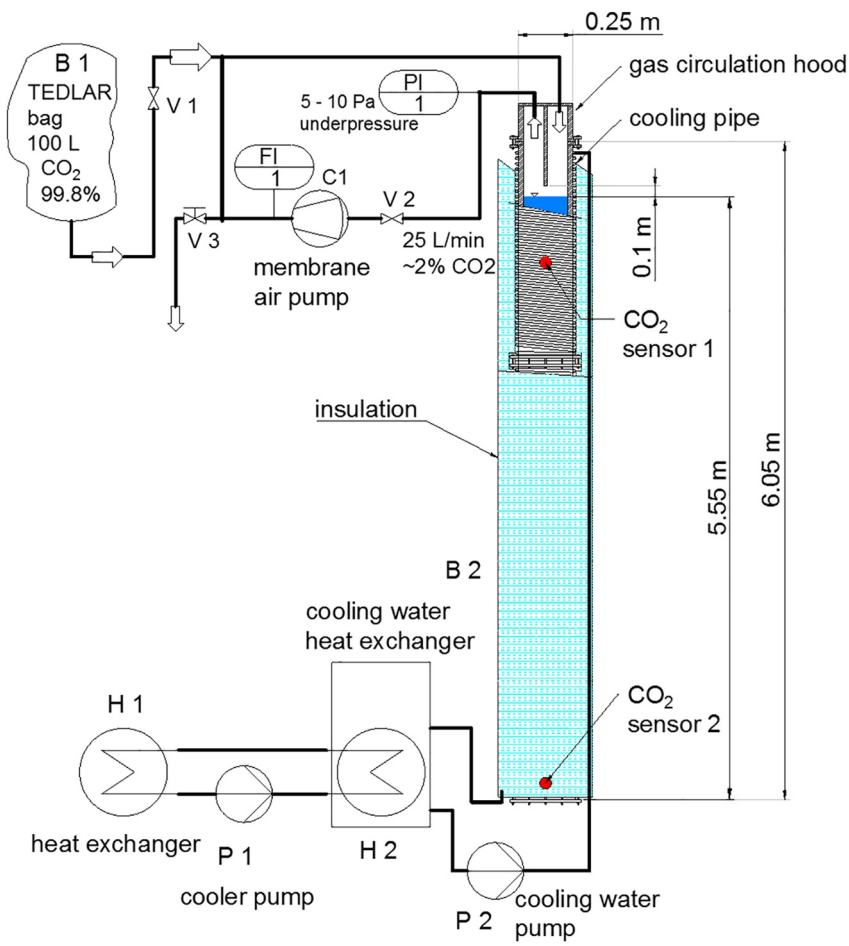

Figure 2. Stagnant water column: process diagram of the experimental setup.

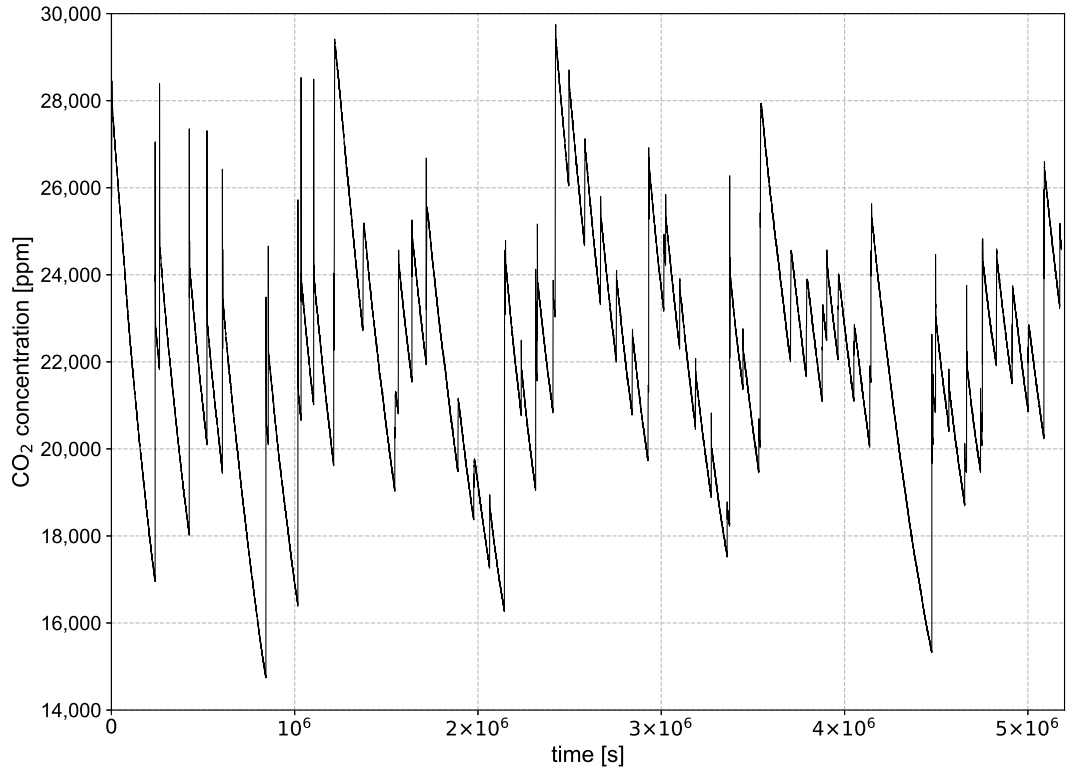

Figure 3. Measured and already corrected CO_2 concentration in air over time in the head space of the column as obtained from intermittent CO_2 additions.

The gaseous CO_2 concentration was continuously monitored and registered by a CO_2 sensor. We started with manually inducing the CO_2, when the monitored gaseous CO_2 concentration in the head space decreased to values below 1.5%. Later on, we also used a time clock to trigger the intermittent feedings. Resulting concentration curves are shown in Figure 3. The water table was located 10 cm below the skimming wall's edge at a height of 5.55 m from the bottom of the column. For a continuous monitoring of the CO_2 concentration in the water, two sensors were installed below the water surface; the upper one at 1 m below the water level and the lower one at 0.15 m above the ground. The upper one was operated between 1,020 and 1,080 hPa absolute pressure, the lower sensor was operated between 1,460 and 1,520 hPa. Generally, various configurations for the measurement of CO_2 in the aqueous phase are found in the literature (e.g., Bell et al., 2007; Camilli & Duryea, 2009; Cioni et al., 2007; Johnson et al., 2010; Kana et al., 1994). For long-term monitoring of CO_2 concentrations, we applied the direct CO_2 measurement subsequent to water-gas partitioning by membrane-separation techniques (De Gregorio et al., 2011; Johnson et al., 2010; Strauch et al., 2020; Zimmer et al., 2011). The gas permeability through polymeric membranes is well constrained (e.g., Barrer & Chio, 1965; Berean et al., 2014; Kjeldsen, 1993; Merkel et al., 2000; Pinnau & He, 2004; Raharjo et al., 2007; Scholes et al., 2009; Schultz & Peinemann, 1996) with the overall concept that only gaseous components pass through polymeric membranes by a solution-diffusion mechanism (Javaid, 2005; Stern et al., 1987), but no liquids. In equilibrium between feed and permeate, the gaseous permeate can then be analyzed using a conventional gas analyzer. Here, we used PVC-covered Vaisala GMP252 infrared gas sensors (factory-calibrated 0–20,000 ppm, accuracy ± 1.5%) at both water depths and the same sensor without PVC-covering at atmospheric pressure conditions in the gas above the water table. The water-proof but gas-permeable PVC cover of 1.4 mm thickness has a CO_2 permeability of about 15 barrer (Kjeldsen, 1993) (1 barrer = 1×10^{-10} ml(SPT)/(s cm cmHg) = $7.500\,6 \times 10^{-18}$ m^3 s/kg), which allows for a fast establishment of equilibrium between the inner gaseous atmosphere of the sensor and the surrounding aqueous environment. The sensors' response time was determined in a certified check gas with 5,200 ppm CO_2 at 0.1 MPa. After about 1 hr exposure time, the equilibrium was established. The sensors require 24 V power which is supplied via a 10 m DC power cable from an external source. Signal wires inside the same cable serve for data transmission to a data-acquisition system (ADL-MX Advanced Datalogger). A self-vulcanization tape (3M) was used for a water-proof

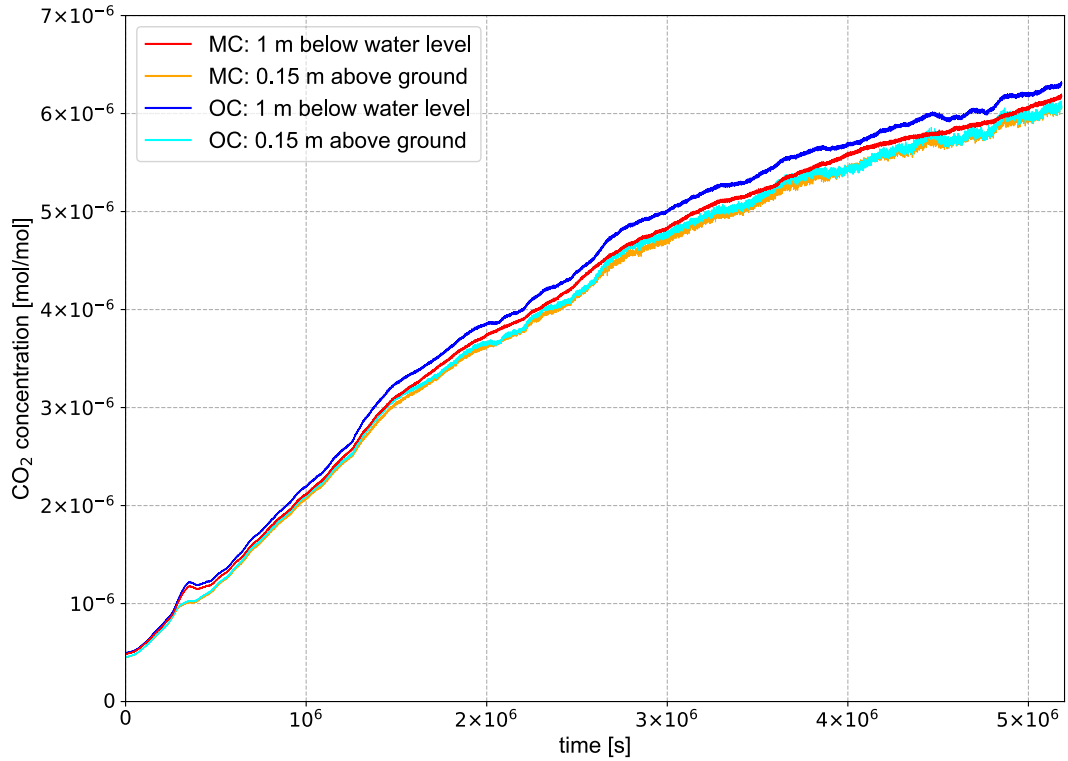

Figure 4. Corrected CO_2 concentration in the water column 1 m below water level and 0.15 m above ground, OC (own correction): red and orange are the concentrations corrected with the own compensation, MC (manufacturer correction): blue and light blue are the concentrations corrected with Equation 1 as provided by the manufacturer.

sealing of the PVC cover and the cable-to-sensor connection. The Vaisala sensors are supplied by the manufacturer with certificates of calibration. For assessing the accuracy of the measurements subsequent to covering, a linear calibration curve was determined using air and check gases with certified CO_2 concentrations of 3,000 and 5,200 ppm, respectively. For the continuous in-situ measurement of dissolved CO_2, the prepared sensors were vertically lowered with the power cable to their defined positions in different depths of the water column.

The sensors were calibrated by the manufacturer at an atmospheric pressure of 1,013 hPa and a temperature of 25°C. Therefore, the CO_2-concentration signal provided by the sensors requires correction for temperature and pressure deviations. Temperature correction is given in the manufacturer's data sheet with ±0.05% of reading/°C deviating from the calibration temperature. As in Johnson et al. (2010), temperatures below calibration temperature require an correction by 0.05% of reading/°C et vice versa. The pressure correction given by the manufacturer is ±0.015% of reading/hPa. After personal communication with the manufacturer we note that typically these probes are used at atmospheric conditions, while we apply it here to conditions in 5.40 m water depth. Since the deviation from calibration pressure is much higher than for typical atmospheric fluctuations, the manufacturer has provided us with the following equation for pressure and temperature compensation:

$$c_{\mathrm{corr}} = c_{\mathrm{meas}} \cdot 1,013 \ \ \mathrm{hPa} \cdot (T/(298 \ \ [\mathrm{K}] \cdot p)). \tag{1}$$

c_{corr} is the corrected and c_{meas} the measured CO_2 concentration of the sensor respectively in ppm or %. T is the temperature in Kelvin and p the pressure in this equation here in hPa during the measurement. In addition, we decided to increase confidence in the pressure correction by producing our own compensation curves and corrections. For this purpose, a measuring pipe was set up which was pressurized with ambient air (≈400 ppm) from 0 hPa to 1,000 hPa overpressure. The results of these measurements can be seen in Figure B1. The deviations at operating pressure of the insitu sensors can now be used for calculating a correction factor, which is 0.124 0 for the sensor at 1 m below water surface and 0.418 1 for the sensor at 0.15 m from the bottom. We apply this correction factor with the temperature correction (±0.05% of reading/°C) mentioned at the beginning of this paragraph. As will be shown later on, our own compensation factors match very well with Equation 1.

For evaluating how the total CO_2-entry rate into the water, $J_{in}^{CO_2}$, relates to a hypothetical purely diffusive rate (in the absence of density effects), we use the dimensionless Sherwood number (Sh). Sh is accordingly defined here as

$$\mathrm{Sh} = \frac{J_{in}^{CO_2} H}{D \Delta \varrho}. \tag{2}$$

We evaluated $J_{in}^{CO_2}$ from the numerical simulations, see Section 2.3. $H = 5.55$ m, the height of the water body (see Figure 2), is used as the characteristic length scale. D is the diffusion coefficient, where we use the same value of $D = 2 \times 10^{-9}$ m^2/s as in Class et al. (2020). $\Delta\varrho$ is the density difference due to dissolved CO_2 concentrations with densities calculated by using Equation A5 at 10°C. We calculated $\Delta\varrho$ by inserting the concentrations at the water table as the upper value, and for the lower value, we used the CO_2 concentration at 0.15 m from the bottom, corresponding to the position of the lower sensor. The calculations for the Sherwood number are also shown in the published data set related to this article (Class et al., 2021).

For maintaining a constant and defined water temperature, the column was insulated (Rockwool panel, 90 mm thickness, aluminum coated, heat conductivity 0.035 W/(mK)) and continuously cooled to 10°C. A circulation cooler (Lauda WK 1200, 1.2 kW cooling power) permanently provided a 10°C cold water flow in a 100 m long cooling pipe (Georg Fischer, JRG Sanipex MT, 26 mm OD × 20 mm ID, thermal conductivity 0.43 W/(mK)) that was spiral-wrapped around the column. The cooling system's sufficient capacity can be explained with a few considerations. The heat flux Q through the cooling-water pipe, the wall of the column, and the insulation can be estimated as

$$Q = \lambda \frac{2\pi l}{\ln(r_o) - \ln(r_i)} (T_i - T_o), \tag{3}$$

with λ representing the materials' heat conductivity, l the height of the column, r_i, r_o the inner and outer radius of the column, and T_i, T_o the inner and outer temperatures. The heat flow through the insulation is then obtained as ≈31 W for $T_i = 10$°C in the pipe and $T_o = 25$°C ambient temperature. The theoretical heat-transfer capacity of the cooling pipe of $l = 100$ m length is ≈13.4 kW. The heat transfer through the walls of the column is calculated to be 357 W. The circulation cooler provides a heat flux of 1.2 kW in maximum. The heat transfer is limited by the heat flux through the walls of the column. The cooler is safely operated at ≈20% of its capacity. The installation is illustrated in Figure 2.

2.2. Experiment: Results

Figure 3 provides the continuously monitored, and already corrected CO_2 concentration (ppm) in the gas phase in the head of the column. The fluctuations are a result of the intermittent additions of CO_2 into the head space. Realistic cave-air conditions also show fluctuations, but we did not attempt to imitate representative cave-air fluctuations. The aim was simply to provide a characteristic average concentration of about 20,000 ppm. The effect of the monitored fluctuations in the gas concentrations on the measurements in the water compared with a constant gas concentrations is quantified in numerical simulations, see Section 2.3.

Figure 4 shows corrected experimental data of the two in-situ sensors over time. The measured and temperature/pressure-corrected data of CO_2 concentration are then converted into x_{CO_2} in mol CO_2/mol water via Henry's law (Equation A4) and $H_{aq,CO_2} = 9.37 \times 10^{-4}$ mol CO_2/mol H_2O·atm in order to use this unit for the comparison with numerical simulations. At the start, both sensors for both corrections show a concentration of $x_{CO_2} \approx 0.4 \times 10^{-6}$ mol/mol, which corresponds well to an equilibrium with ambient air at $x_{CO_2} \approx 400$ ppm and 10°C water temperature. After initiating the CO_2 influx into the head space, the first increase in CO_2 concentration can be observed almost simultaneously for both depths after $t \approx 10^5$ s. A peak in concentration appears after $t \approx 3 \times 10^5$ s, which seems to be an anomaly. This anomaly is mitigated in the second sensor and the question is whether or not this can be attributed to the density-induced fingering in the water column. It would make sense, but we cannot assess it with certainty. Beyond that, the concentration increases monotonously with time while the slope decreases with time. Stronger noise in the data can be seen in the second half of the plot for the deeper sensor. Also, both concentration signals are slightly drifting apart from each other over time. Beyond the time of 60 days, we expect that the curves further decrease in their slope until finally a state of equilibrium with the given CO_2 concentration

at the water table in the head space is reached. Since the concentration difference is the driving force and gets smaller with time, this will go on for a longer period.

In Table 1, we provide parameters from an analysis of water samples from before and after 60 days. One may consider, for example, the difference in TIC, which is 4 mg/l. Using a molar mass of 12 g/mol for C and 44 g/mol for CO_2, this corresponds to 14.67 mg/l additional CO_2 in the later water sample. Converting this into added mole CO_2 per mole H_2O yields then about 6×10^{-6} mol/mol, which is in reasonable agreement with the values we see in Figure 4. Alternatively, using the Bjerrum plot and the measured pH-values, we could also estimate the CO_2 concentration from the TIC contents. At pH = 8.16, there is CO_2 in the order of only 1%, while at pH = 7.4 it approaches close to 10% of the TIC. This would end up with about 4.6×10^{-7} mol/mol before the experiment and about 5.2×10^{-6} mol/mol after 60 days. Thus, we conclude that, although not being able to exactly figure measurement uncertainties, we have confidence that the observed CO_2 concentrations are reliable. In the next section, we describe the comparison with numerical simulations, where we use a model that does not consider water chemistry and pH, but only CO_2 dissolving according to Henry's law. Thus, the model does not account for the amount of newly dissolved CO_2 that transforms into HCO_3^-, which we estimate to be in this case in the order of 13%, obtained from $\frac{6-5.2}{6}$, see the estimated numbers above. We should, thus, expect a slight overestimation of the predicted CO_2 concentrations.

2.3. Comparison With Numerical Simulations

A modeling study is performed for interpreting the experimental results and increasing confidence in both measurements and model. In the model, the column is idealized as a 2D setup. For capturing the effects that trigger the fingers at the top of the water body, a grid refinement in the upper parts is important for modeling the density-driven dissolution (Class et al., 2020). It is important to resolve the formation of the layering due to CO_2-enriched water at the top and the resulting instability which then leads to fingering. Thus, the topmost 50 cm of the model are graded vertically and discretized with 100×23 cells in vertical and horizontal direction, thus resulting in a minimum cell size at the top boundary of $\delta x = 0.001\,6$ m and $\delta z = 0.01$ m. For the remaining 5.05 m vertical length of the column, the mesh is regular with 505×23 cells and $\delta x = \delta z = 0.01$ m. The numerical model used for this study is the same isothermal model as in Class et al. (2020). The model solves the continuity equations for the components water and CO_2, both present in the aqueous phase, as well as the Navier-Stokes equations. For details, we refer to Appendix A. As mentioned before, the model neglects water chemistry and pH.

In the first instance, we ran two different realizations for the top boundary CO_2 concentration. In one realization, we assumed a constant CO_2 concentration at the top boundary, and, therefore, the mean concentration of the 60 days time period was used, i.e. $c_{CO2} = 20,707$ ppm in the column's head-space atmosphere. Using Henry's law, the dissolved CO_2 concentration can be calculated, and it is then implemented as Dirichlet boundary condition $x_{CO2} = 1.949\,8 \times 10^{-5}$ mol/mol at the top. In the second realization, the fluctuations of CO_2 concentration as shown in Figure 3 were considered in order to assess, in comparison with the first realization, the influence of the intermittent regime of CO_2 additions. Therefore, the mean CO_2 concentration was calculated for ten-minutes intervals and tabulated. For each time step, the model can then take the associated mean value as the top boundary condition. The time-step size was limited to 10 min maximum, while, as controlled by the applied non-linear Newton solver and the corresponding convergence criteria (Koch et al., 2020), time steps were mostly between 60 and 300 s. Aqueous CO_2 concentration from the simulation were compared with the experimental results at the corresponding sensor locations.

Figure 5 shows the comparison of the measured data with different realizations of simulated curves; the top chart shows the results for 1 m water depth and the bottom chart the results in 0.15 m from the bottom of the column. The red curve (1 m depth) and the orange curve (0.15 m from the bottom) represent the experimental data, thus the same as those with manufacturer's correction in Figure 4. Green shows the simulation results with constant CO_2 concentration assumed at the top boundary, while the purple curve was obtained when the measured data in the column's head space were used as boundary condition. The black line represents a realization with another Henry coefficient applied to the gas-water interface and will be discussed later on in this section.

The simulation results obtained with constant CO_2 atmosphere (green) and with the fluctuations as in the experiment (purple) do not show significant differences and are almost on top of each other. The noise in the simulated curves is a result of the fingering, while the time delay in the sensor signal due to the required equilibration time

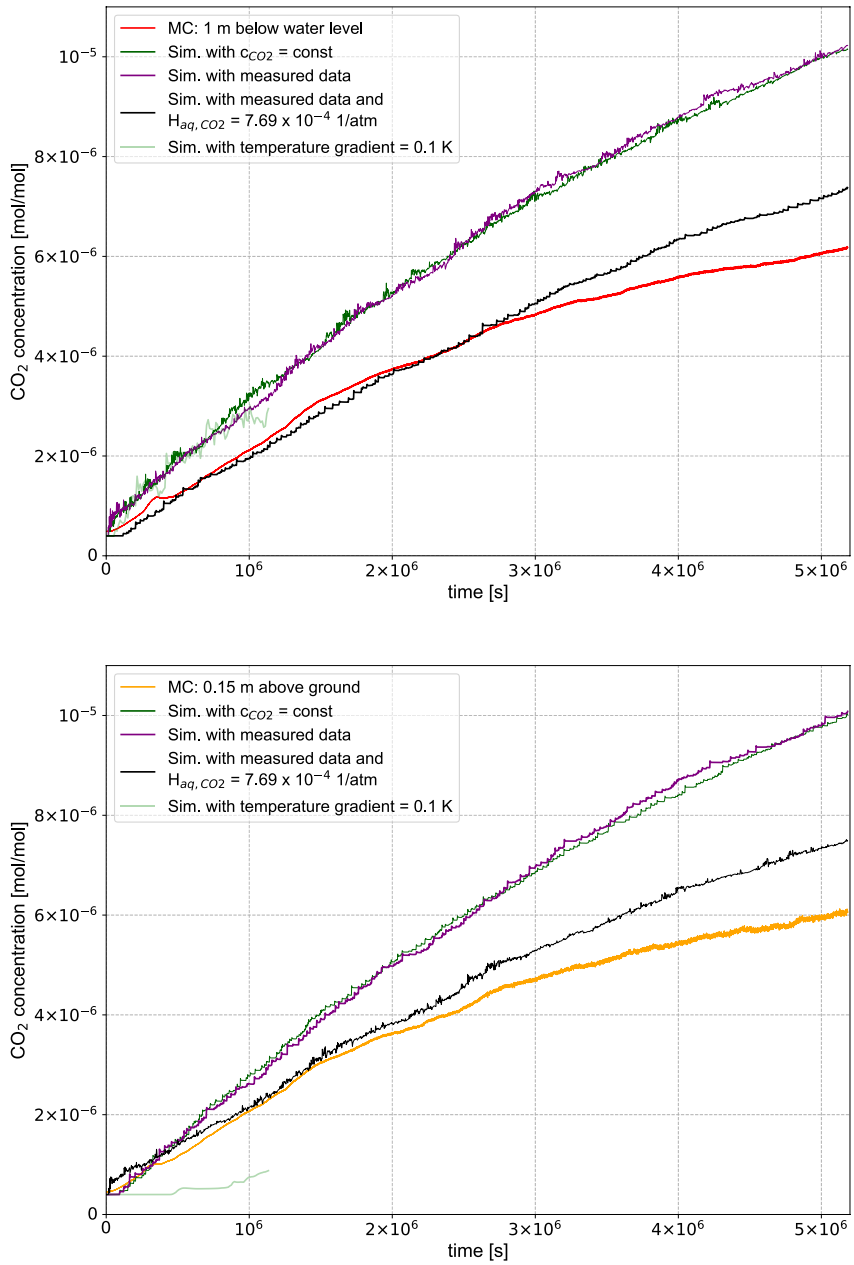

Figure 5. Comparison of experimental data with different realizations of numerical simulations; top figure shows curves in 1 m water depth, bottom figure in 0.15 m from the bottom. Please find detailed explanations in the text.

prevents much of the resolution of these fluctuations in the measured curves. This is inherent to the measurement setup and not worrying. However, the simulation results deviate from the experimental data systematically. There are different sources of error/uncertainty to explain this. We mentioned already above, that we expect some overestimation of simulated concentrations in the order of 13% since the model neglects water chemistry. This is clearly not sufficient to explain the observed difference. We believe that one major point could be due to a non-perfect cooling at the gas-water interface. As shown in Figure 2, cooling and insulation did not include the lid, which holds around half of the column's air space. CO_2 was pumped into the lid at ambient temperature and cooled down only on its way to the water surface. If this path was not sufficient to cool the air to water temperature at the water table, then our assumption of the Henry coefficient to calculate how much CO_2 is dissolved is no longer correct. Gas solubility in liquids decreases with increasing temperature. To test this hypothesis, we have run one simulation where we assumed a Henry coefficient corresponding to a higher temperature at the water

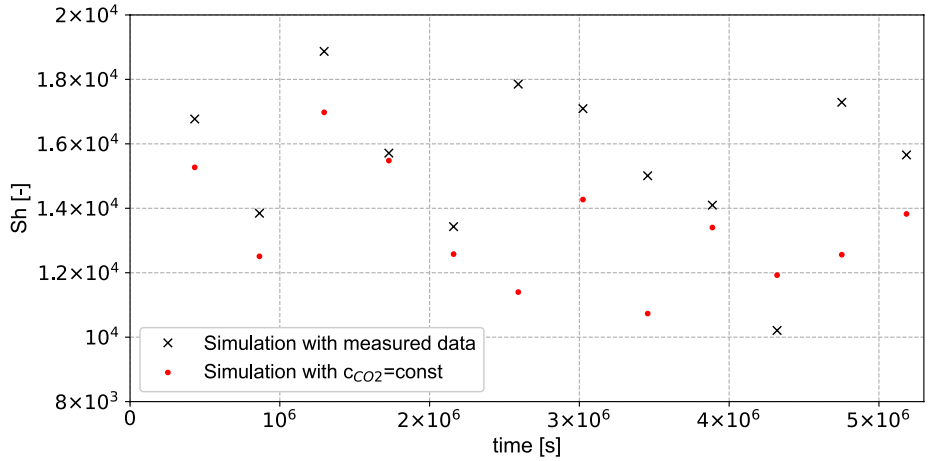

Figure 6. Sherwood numbers of the model realizations with measured CO_2 data and with c_{CO_2} = const. in the head space as top boundary condition, evaluated at time intervals of 5 days.

table. Note, that we did not attempt to calibrate the model, but we primarily aim at demonstrating the potential of this hypothesis to explain the observed deviation. We used a Henry coefficient of $H_{aq,CO_2} = 7.69 \times 10^{-4}$ mol CO_2/mol H_2O·atm and with that obtained the black line in Figure 5. This value corresponds to a temperature of $T = 16.8$°C. Clearly, the black line shows much better agreement with the measurements in 1 m depth and still significantly better agreement in 5.40 m depth.

For an evaluation of the Sherwood number, see Equation 2, we evaluated the influx of CO_2 at the top boundary as obtained from the numerical simulations. The result serves as an indicator for how large the actual CO_2 inflow is relative to a purely diffusive flow. It is shown in Figure 6 at time intervals of 5 days. Whereas the influx of CO_2, in terms of $J_{in}^{CO_2}$, decreases over time due to a higher CO_2 concentration in the water and the associated smaller $\Delta\rho$, the Sherwood number seems to show no clear tendency, thereby underlying a zig-zag pattern at the evaluated points. The zig-zag pattern is due to the random nature of the vertically oriented fingering, which is not fully resolved in time in this plot. The fluctuations of $J_{in}^{CO_2}$ occur when convective fingers draw CO_2 downwards and more CO_2 dissolves again at the water surface. In turn, this causes $J_{in}^{CO_2}$ to re-increase or to decrease while new fingers are just forming. The hypothetically assumed purely diffusive flux would scale solely with the concentration gradient. However, the concentration is also included in the Sherwood number via the $\Delta\rho$-values. Thus, we can infer that the influence of the density-driven flux relative to the purely diffusive flux does not lose significance as the experiment proceeds. The absolute CO_2 fluxes decrease over time, but the ratio of density-driven versus diffusive fluxes does not shift toward diffusive, because both the density gradient and the concentration gradient decrease.

Let us finally check our assumption of having isothermal conditions due to the cooling and insulation of the water column. We elaborated above that there are deviations from isothermal conditions in the head space that affect the very top of the water body, but the question remains if the rest of the water column was without a temperature gradient during the experiments. How would fingering patterns be affected by a temperature gradient? Running numerical simulations allows for finding out how temperature gradients would change the signals of CO_2 concentrations. To do so, we consider now a double-diffusive problem, since diffusion and thermal conduction are both diffusive in nature. According to the temperature conditions in the lab during the experiment and hypothesizing non-perfect cooling, we choose a scenario where warm and CO_2-rich water is located over colder water with less CO_2. This regime would favor the formation of stable fingers in comparison with a single-diffusive problem without a temperature gradient, which would predominantly form convection cells (Hage, 2010; Kellner, 2016). The CO_2-rich, warm fluid would sink and, due to local instabilities, would form fingers that spread downwards. Due to the high thermal conductivity of water, the originally higher temperature within the fingers would quickly equilibrate with the colder water further below. Since CO_2 diffuses in water much slower than heat, the concentration within a finger would remain almost constant meanwhile, resulting in more stable fingers that can develop further downwards. To illustrate this in numbers we performed two different non-isothermal simulations, with temperature differences of 0.1 and 0.2 K between top and bottom of the water body. A thermal-energy balance equation

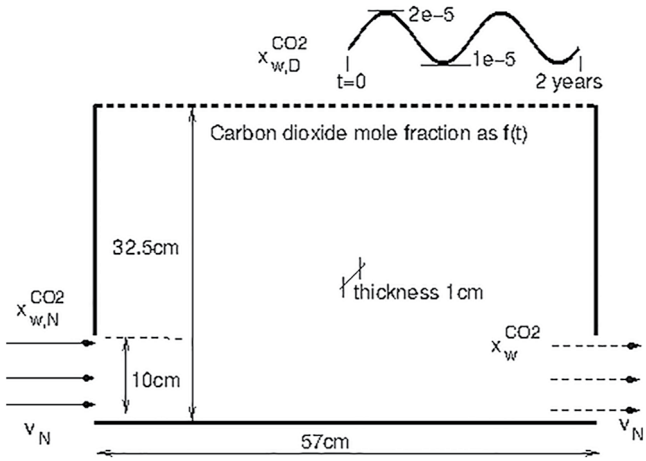

Figure 7. Dimensions and boundary conditions of the 2D simulated flume-scenario with background flow.

is solved in addition, which significantly increases computational time, so we did not run the full period of 60 days. The results of the 0.1 K-non-isothermal simulation are shown in Figure 5, easily discernible as the curves which are shorter in time. It is clearly noticeable that the non-isothermal simulations predict significantly smaller concentration of CO_2 at a given time compared to the experimental data and the isothermal simulations. This is even more distinct for the 0.2 K case (not shown). In these simulations with temperature gradients, the formation of a stable fingering regime and the slow propagation velocity of fingers slows down the CO_2 transport in the column and results in a reduced concentration of CO_2 at the bottom compared with the measurements. Since already small temperature gradients would lead to strong deviations from what we observed in terms of CO_2 concentrations, we are now confident that temperature effects within the water body, separate from the above-mentioned presumably not perfectly cooled head space, are negligible for interpreting our observed data.

3. Generic Scenario With Background Flow in a Small Laboratory Flume

Using a generic lab-scale setup for a simulation study, we highlight now the role of background flow, in other words: forced convection, on the occurrence of distinct CO_2 fingering regimes. Recently, Michel-Meyer et al. (2020) presented an experimentally supported study on the role of water flow and dispersion in density-driven dissolution related to geologic storage of CO_2. They concluded from their results that dissolution rates do not significantly decrease with increasing background flow even though fingering regimes are then getting suppressed. While the study of Michel-Meyer et al. (2020) refers to processes in porous media, we remind that our focus here is primarily on open water bodies, where we have no such experimental data available. The modeling study presented below builds on a small experimental laboratory setup, previously used by Class et al. (2020) under stagnant conditions for validating the numerical Navier-Stokes model which is briefly explained in Appendix A.

3.1. Model Setup and Methods

The setup includes a water-filled flume, confined at the front and the back by two parallel glass plates with 1 cm distance in between. The flume is 57 cm wide and 32.5 cm high (Figure 7). Class et al. (2020) applied different, but in each calculated scenario constant CO_2 partial pressures in the gas phase at the open top of the water-filled flume to trigger density-induced dissolution. We use the same isothermal numerical model as before, solving Navier-Stokes and continuity equations for water and CO_2, and again we refer to Appendix A. The model domain is discretized with a regular mesh, 54 cells in vertical and 95 cells in horizontal direction; thus, the discretization length is in both directions 0.006 m. The maximum time-step size is 30 s, which is in this case not limited by convergence criteria of the applied Newton solver.

As initial condition, the water in the flume has a very small concentration of dissolved CO_2, expressed by a mole fraction of $x_w^{CO2} = 2.5 \times 10^{-7}$. The boundary conditions are illustrated in Figure 7. The bottom boundary and the upper parts (>10 cm from the bottom) of the lateral boundaries are no-flow boundaries for water. An inflow velocity of water, v_N, with a constant dissolved CO_2 mole fraction of $x_{w,N}^{CO2} = 1.5 \times 10^{-5}$ is imposed horizontally at the lower part of the left lateral boundary, while the same amount of water flows out at the lower part of the right lateral boundary with the outflux of dissolved CO_2 being dependent on the local mole fractions x_w^{CO2}. The value of 1.5×10^{-5} was measured by us on 10 April 2021 in water collected in a karst cave (Laichinger Tiefenhöhle) on the Swabian Alb, a karstic mountain range in Southern Germany. Comparable and even higher values are mentioned by Serrano-Ortiz et al. (2010). At the top boundary, we imposed a seasonally varying CO_2 concentration $x_{w,D}^{CO2}$ as Dirichlet condition, with a sine-wave function that has 1×10^{-5} and 2×10^{-5} as its minimum and maximum values. We assume that this is in equilibrium with a gaseous CO_2 concentration at the water table. Applying this sinus curve is motivated from seasonal variations of biogenic CO_2. Thus, the CO_2 concentration at the influx, $x_{w,N}^{CO2}$ can be understood as a yearly averaged concentration. We consider this choice as adequate and reasonable for demonstrating the effects we intend to show with this generic setup. The plume thickness is 1 cm, and wall

friction is considered accordingly by a thickness-dependent drag term in the Navier-Stokes equation, see Appendix A. Hence, the model solved in 2D can be viewed as a pseudo-3D approach. Class et al. (2020) showed that this approach was able to reproduce experimental results in stagnant water satisfactorily.

We ran realizations of this numerical-modeling scenario with varying values for v_N and computed the CO_2 influx rate from the top boundary, J_{in}^{CO2}, as a model output. To evaluate this influx rate relative to the forced advective flow, we use the dimensionless Sherwood (Sh), Péclet (Pe), and Rayleigh (Ra) numbers. Sh was introduced before in Equation 2 and relates the effective influx J_{in}^{CO2} to the purely diffusive flux rate. In this case here, we have $H = 0.325$ m (see Figure 7), as the characteristic length scale. For $\Delta\varrho$, the characteristic density difference due to dissolved CO_2 concentrations, we employ here a calculation of water density at 8°C according to Equation A5. With $x_{w,D}^{CO2} = 2 \times 10^{-5}$ and $x_{w,N}^{CO2} = 1.5 \times 10^{-5}$, this yields $\Delta\varrho = 2 \times 10^{-3}$ kg/m^3. Different than scenarios in geologic CO_2 sequestration where a plume of CO_2 segregated by gravitation rests on top of the brine, thus providing a constant value of dissolved concentration there, our study features a fluctuating CO_2 concentration to obtain the flux rate J_{in}^{CO2}. Therefore, choosing a characteristic value for $\Delta\varrho$ is not straightforward. We decided to evaluate these dimensionless numbers after 1×10^7 s, which is about the time when the maximum concentration is reached, see the results section further below.

Pe represents the ratio of advection versus diffusion, expressed here with the horizontally oriented v_N as

$$\mathrm{Pe} = \frac{v_N H}{D}, \tag{4}$$

and Ra is a measure for the instability, according to Green and Ennis-King (2018) given by

$$\mathrm{Ra} = \frac{k\, g\, \Delta\varrho\, H}{\mu\, D}. \tag{5}$$

g is the gravitational acceleration, μ the dynamic viscosity of water at 8°C, 1.35×10^{-3} kg/m s. Since this definition of Ra is taken from porous-media literature, k represents the permeability, which is approximated here as $k = b^2/12$ with thickness $b = 0.01$ m.

3.2. Results

Let us keep in mind our overall goal of substantiating the claim that density-driven dissolution of CO_2 is a relevant mechanism for replenishing karst waters. This directs our focus toward small background-flow velocities, so to speak gently forced convection, since at higher flow velocities the occurrence of fingering regimes is suppressed (Michel-Meyer et al., 2020). In analogy to studies related to thermal convection versus diffusion, we can distinguish the influence of natural convection due to density difference and forced convection by lateral flow. Figure 8 (left) shows the total influx of CO_2 through the top boundary plotted over a time of two years for different lateral flow velocities v_N. Dividing this value by the length of the flume, we obtain the value of J_{in}^{CO2} as used in calculating the Sh number. It is evident that in periods where the CO_2 concentration at the top boundary is rising (see Figure 7), the oscillatory behavior of the curves has to be attributed to fingering regimes. This corresponds to the phenomenon of natural convection, which is suppressed for larger values of v_N as the curve for $v_N = 1 \times 10^{-4}$ m/s clearly shows by its smoothness. The curves for smaller lateral velocities show that the influx during increasing CO_2 concentrations at the top boundary, i.e. during spring and summer seasons, is significantly higher than the outflux back to the atmosphere in winter periods. A cumulative net influx of CO_2 into the water over time is clearly obtained, which increases with the lateral flow velocity. In contrast, for lateral flow velocities above a critical threshold, where fingering regimes are suppressed, the dominant forced convection leads to a cumulative in-/outflux over time which is about zero. The CO_2 inflow is small for small v_N since the density difference diminishes when dissolved CO_2 is not removed by the lateral flow. There is obviously an optimum v_N, which is around 1×10^{-5} m/s for this particular setup.

Figure 8 (right) plots the CO_2 inflow, expressed by the Sh number, over the ratio of Pe/Ra. A small Pe/Ra ratio corresponds to small v_N and, thus, to curves with small velocities in Figure 8 (left). Note that the plot on the right contains points from simulations which are not all shown in the left plot. We ran a few more simulations in the region around Pe/Ra ≈ 1. As known from heat-convection studies (e.g., Lai & Kulacki, 1990, 1991), there is a non-monotonic behavior of Sh for Pe/Ra with a local minimum around 1. For Pe/Ra>1, the forced-convection

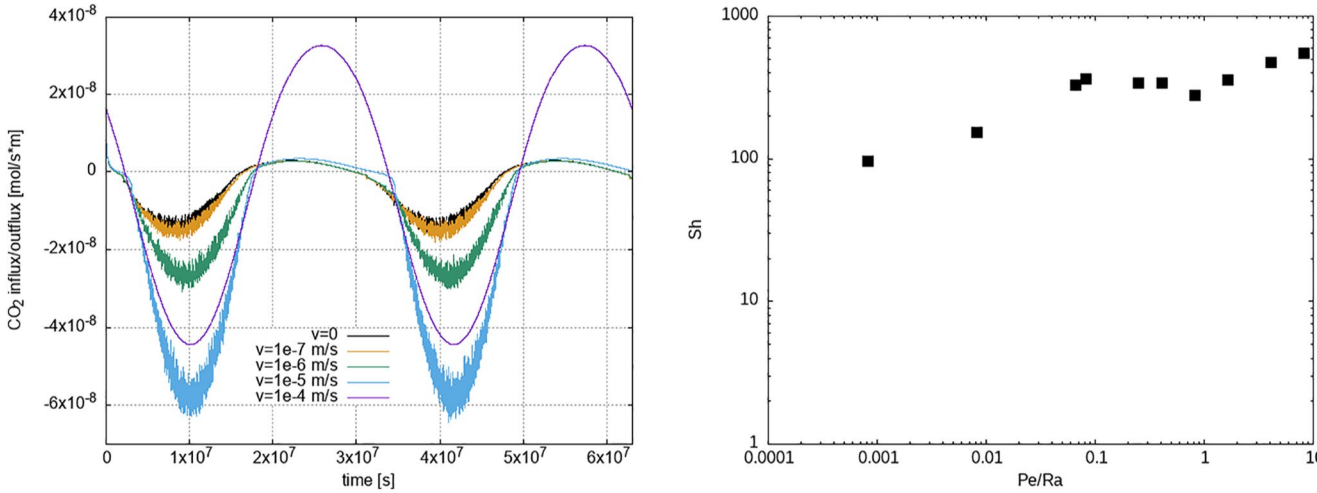

Figure 8. Left: CO_2 inflow (negative values) and outflow (positive) rate over two years at the top boundary of the flume, shown for scenarios with different in-/outflow velocities imposed at the bottom 10 cm of the lateral boundaries. Oscillatory curves indicate fingering regimes. Right: Mass influx evaluated at 10^7 s, expressed by Sh and plotted over Pe/Ra; note that not all points are represented as curves in the left plot.

regimes dominate and mass transfer further increases. The local minimum at Pe/Ra $\approx$ 1 is confirmed by the simulation results. Fingering regimes, our focus of interest, occur for Pe/Ra<1. The decrease of Sh for very small values of Pe/Ra is due to the accumulation of CO_2 in the water body, which is not sufficiently diluted by the smaller enforced lateral flow. Unlike in geologic CO_2 sequestration scenarios (Green & Ennis-King, 2018), we don't see here for small Pe/Ra ratios a steady flux regime for J_{in}^{CO2}. This has two reasons: first, the boundary condition ($x_{w,D}^{CO2}$) driving the fingering regime is not constant in time; second, the height of the setup is small here and for small Pe/Ra the CO_2 quickly accumulates in the flume and diminishes the density difference.

Figure 9 displays plots of CO_2 mole fractions at 1×10^7 s, i.e. the time at which the dimensionless numbers were calculated above. The dark blue color corresponds to the value of $x_{w,N}^{CO2}$ (inflow concentration) and the dark red to the value of $x_{w,D}^{CO2}$ (maximum concentration at the top boundary). For v_N values of 1×10^{-7} m/s, 1×10^{-6} m/s, and 1×10^{-5} m/s, fingering regimes can be easily recognized. For $v_N = 1 \times 10^{-4}$ m/s, there is no fingering regime anymore, only some minor effect of downward movement at the very left and very right of the domain. With increasing v_N, the blue colors tend to dominate over the red. At small v_N, the blue color shows a vertically upward tendency which can be attributed to the density difference of the water. The low-concentrated water flowing in is lighter than the high-concentrated water and the forced convection is weak relative to this upward drive. This changes for higher v_N toward a domination of forced convection.

4. Discussion and Conclusions

The findings of this study may be classified on two different levels. On the one hand, we have provided experimental and numerical and, thus, quantified results on CO_2 dynamics in water exposed to well-defined concentrations of CO_2 in the gas phase above. On the other hand, we pursue an agenda of promoting a discussion on density-driven dissolution as a potentially relevant mechanism in karst systems in general. In fact, we are wondering why this did not get much attention so far, in particular as density-driven dissolution is known since many years as one of the major trapping mechanisms in geological storage of CO_2 (IPCC, 2005). Evidently, the CO_2 concentrations in caves and karst systems are much smaller than in geological storage. Thus, it requires quantification to evaluate the potential relevance of density-driven dissolution for karst systems, which is what we provide with this study. We come back to the research questions formulated in the introduction.

What do we know about CO_2 dynamics in water bodies exposed to fluctuating CO_2 partial pressures at the water table? Can we measure it? And do we have numerical models that are capable of describing these processes?

We were able to measure CO_2 dynamics in a stagnant water column exposed to fluctuating CO_2 partial pressures at the water table. The design of our experimental setup allows for continuous and accurate measurement

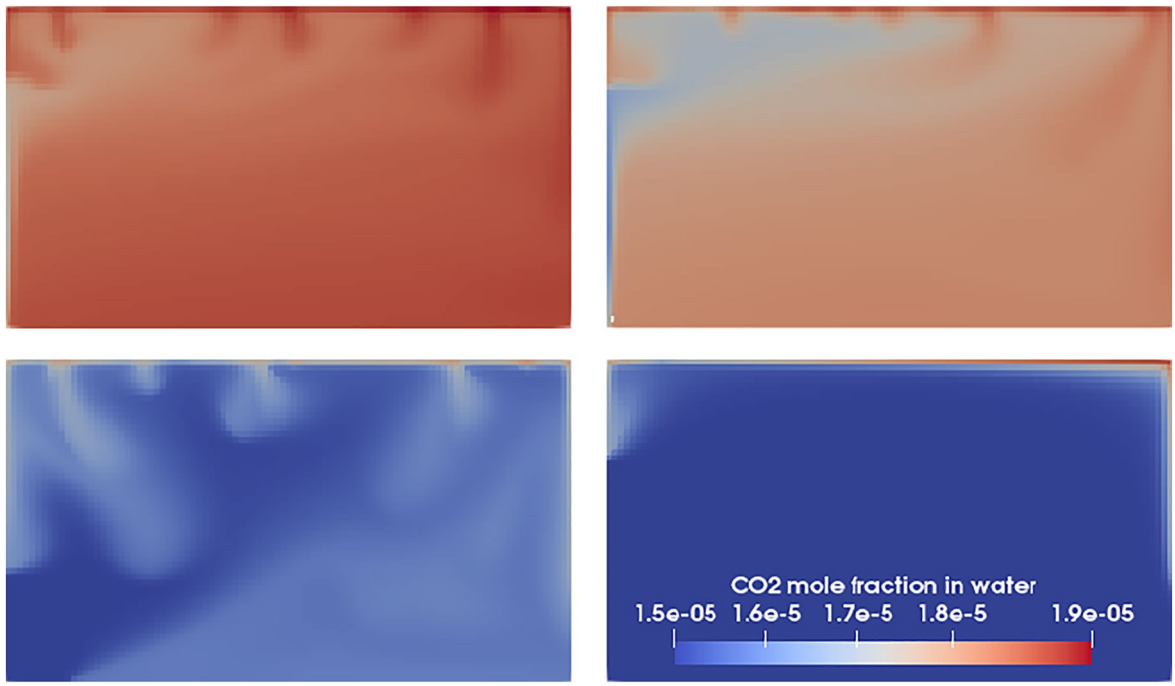

Figure 9. Plots of CO_2 mole fractions at 10^7 s for different forced horizontal background flow velocities; at this time, CO_2 concentration at the top boundary is near its maximum. From top left to bottom right: $v_N = 10^{-7}$ m/s, 10^{-6} m/s, 10^{-5} m/s, 10^{-4} m/s. Legend: in all plots, dark blue represents a value of 1.5×10^{-5}, dark red represents 1.95×10^{-5}.

of concentrations of dissolved CO_2 in different water depths. The measured values are gas-phase concentrations, which were converted into dissolved concentrations via Henry's law. Starting at a very low concentration, ≈400 ppm - gas-phase equivalent-, and applying cave-like elevated CO_2 concentrations at the water table, ≈20,000 ppm (value confirmed by own measurement and similarly reported also by others (e.g., Serrano-Ortiz et al., 2010)), we can quantify the CO_2 mass transfer into the water over time, which is crucially important to evaluate the potential impact of density-induced dissolution on the replenishment of the water with CO_2. Numerical simulations show very encouraging agreement with the experimental curves in spite of remaining uncertainties related to pressure-dependent correction of the sensor measurements and, in particular in our setup, probably a deviation from perfectly isothermal conditions at the air-water interface at the top of the column. The high measurement accuracy of the in-situ setup in the stagnant water column, that also Johnson et al. (2010) claimed to achieve with a very similar Vaisala sensor setup, is here confirmed by the comparison with numerical simulations. This strengthens confidence that our model can capture the dynamics and, accordingly, it can be used to vary the experimental conditions to include the effect of background flow.

What are the conditions for density-driven dissolution of CO_2 to occur?

We complemented the stagnant water column with a flume scenario where a groundwater background flow was prescribed, i.e. forced advection with a horizontal gradient competes with the naturally occurring convection due to density differences. We could show that our Navier-Stokes model applied to a seasonal cave-like scenario is able to capture the interaction between forced and natural convection. Results showed a local minimum of CO_2 mass transfer for a Pe/Ra ratio around 1. For Pe/Ra larger than 1, forced convection is dominant and density-driven dissolution does not play a major role anymore. Consequently, our interest is on the regimes with Pe/Ra smaller than 1. For very small background flow, mass-transfer rates are sooner or later leveling out since equilibrium between liquid concentration and gaseous concentration of CO_2 will be approached. This is what we see in the stagnant water column. The slope of the increasing CO_2 concentration in Figure 4 is flattening over time. Therefore, in order to keep up the mass transfer of CO_2 from the gas phase into the water, a forced convective background flow is beneficial. The driving force for density-driven dissolution is determined by the present concentration in the water and by the concentration in the gas phase above the water table, i.e. in karst context: at the epiphreatic interface. Since we can imagine an enormous variability of hydrological conditions and scenarios,

one may easily find therein scenarios where there are, for example, intermittent stagnant periods of water tables exposed to seasonally fluctuating CO_2 concentrations in the gas, interrupted by flow during and after infiltration events. For such situations, classical karstification theories do not mention a replenishment of CO_2 in the water during stagnant periods, while we clearly show that within a few months time, water concentrations of CO_2 can approach equilibrium conditions with cave-like CO_2 partial pressures at the water table.

An evaluation of dimensionless Sherwood numbers gives strong indication that the relative influence of density-driven transport of CO_2 versus purely diffusive transport is not strongly dependent on the concentration gradient of CO_2 in water. Even at small differences, density effects are dominating the influx rates of CO_2 at the gas-water interface. We consider this also a significant insight given the large time scales to be considered in karstification.

Can we estimate density-driven CO_2 dissolution rates, for example, in phreatic caves?

We could, for example, calculate theoretical best-case CO_2-entry rates at the gas-water interface based on the Sherwood numbers shown in Figure 8. The highest values occur at Pe/Ra $\approx$ 0.1, which corresponds to a CO_2 cave-air concentration of 2% with a horizontal background flow velocity in the order of 1 m/d. This would allow for $\approx$10 g CO_2 per month and m^2 of gas-water interface as maximum possible CO_2-entry rate contributed by this process.

Is density-driven CO_2 dissolution relevant for karst hydrology, geomorphology, or speleology?

Given the significant entry rates of CO_2 into water bodies under optimal conditions, there is reason to demand for larger-scale and longer-term studies in variable hydrogeological scenarios. It is worth noting that we did not yet thoroughly investigate the limits until when instabilities occur that can trigger density-driven dissolution. This may strongly depend on local hydrogeologic conditions, like heterogeneities, existence of pathways for air into open subterranean water bodies, availability of high-permeable porous media that allow instabilities and significant mass transfer to occur, and also on temperature gradients, which can have stabilizing or destabilizing effects on density-driven dissolution of CO_2. We focused here first of all on karst systems, since there the existence of connected gas-flow paths reaching to karst-water tables is usually given, where triggering of fingering regimes due to instabilities is not limited by small permeabilities.

When Ma et al. (2014) wonder why "a downward CO_2 flux seems to have nowhere to go" and assume that fluctuations of groundwater levels carry dissolved inorganic carbon downward, or when Serrano-Ortiz et al. (2010) postulate "hidden, abiotic CO_2 flows …in the terrestrial carbon cycle", is it possible that density-driven dissolution would assist in explaining and interpreting "anomalous" CO_2 flux measurements? Although we put the focus of this study on karstification and, thus, on the water part of the overall processes at the interfaces between atmosphere, vadose zone, and phreatic zone, we expect that this topic may reach further into discussions of mass fluxes within carbon cycles, also relevant for regional CO_2 budgets or climate modeling.

We suggest and plan to perform long-term measurements in a cave with naturally occurring fluctuations of CO_2 in the cave air and to measure the dynamics of CO_2 concentrations in different water depths. In order to conclude on a potential contribution of density-driven CO_2 dissolution to speleogenesis, the kinetics of the reaction system with carbonates, CO_2, and water needs to be studied in relation to the transport mechanisms. Dissolution of carbonates has an additional effect on density and further changes the natural convection processes.

Appendix A: Numerical Model Used in the Simulations

A1. Governing Equations

Continuity equation for each component $\kappa \in \{w, CO_2\}$:

$$\frac{\partial (\varrho X^\kappa)}{\partial t} + \nabla \cdot (\varrho \mathbf{v} X^\kappa - D^\kappa \varrho \nabla X^\kappa) = 0. \tag{A1}$$

ϱ is the density of the aqueous phase, $\mathbf{v}$ is the velocity vector, D is the binary diffusion coefficient.

Navier-Stokes equation:

$$\frac{\partial(\varrho \mathbf{v})}{\partial t} + \nabla \cdot (\varrho \mathbf{v}\mathbf{v}^{\mathrm{T}}) = \nabla \cdot (\mu(\nabla \mathbf{v} + \nabla \mathbf{v}^{\mathrm{T}})) - \nabla p + \varrho \mathbf{g}. \tag{A2}$$

μ is the dynamic viscosity dependent on temperature, p is pressure, $\mathbf{g}$ is the gravitational acceleration vector.

The model is pseudo-3D. Assuming a parabolic velocity profile along the axis of the omitted dimension, a friction term is applied (Flekkøy et al., 1995):

$$\mathbf{f}_{\mathrm{drag}} = -c \frac{\mu}{h^2} \mathbf{v} \ , \tag{A3}$$

which is added to the right-hand side of Equation A2, with h the domain height in the neglected direction. $c = 12$ considers a height-averaged velocity.

The concentration of CO_2 at the interface between the atmosphere and the water body is calculated as a function of the partial pressure of CO_2 p_{CO_2} (in atm) in the ambient atmosphere by assuming equilibrium between the fluid phases. Accordingly, Henry's law is assumed to be valid:

$$x_{CO_2} = H_{aq,CO_2} p_{CO_2}, \tag{A4}$$

H_{aq,CO_2} (in mol CO_2/mol H_{20}·atm) is the temperature-dependent Henry constant for CO_2 in water.

A2. Numerical Solution

The numerical simulator DuMu^x (www.dumux.org) provides the platform for solving the system of equations. We used for this study the *freeflow Navier-Stokes model* in DuMu^x and the *brineco2* fluid system.

Pressure, concentration (mole fraction) and the velocity vector are selected as primary unknowns for solving the system of equations with a staggered-grid method, that corresponds to a finite-volume method with different control volumes for different equations. The control volumes for the velocity components and the control volumes for the pressure and mass fractions are staggered. This provides a robust and mass conservative scheme without pressure oscillations. All equations are solved fully implicit in time using a Newton method to treat non-linearities. The Newton scheme adapts the time-step size to its convergence with a user-controlled maximum time-step size. For further details on discretization, numerical solution methods, and their implementation, we refer to Koch et al. (2020) or the handbook of DuMu^x (Dumux handbook, 2021).

A3. Density Variation

The partial differential equations are coupled via the density which depends on the CO_2 concentration. We follow here an approach suggested by Garcia (2001).

The density (in kg/m^3) is computed as

$$\varrho = \frac{1}{x^{\mathrm{CO_2}} \frac{V_\phi}{M_T} + x^{\mathrm{H_2O}} \frac{M_{\mathrm{H_2O}}}{\varrho_w M_T}}. \tag{A5}$$

ϱ_w is the density of pure water dependent on pressure and temperature, $M_{\mathrm{H_2O}}$ is the molar mass (in kg/mol) of pure water, while M_T is accordingly obtained from

$$M_T = M_{\mathrm{H_2O}} x^{\mathrm{H_2O}} + M_{\mathrm{CO_2}} x^{\mathrm{CO_2}}. \tag{A6}$$

The apparent molar volume of dissolved CO_2 V_ϕ (in m^3/mol) is calculated as a function of temperature T (in °C) from

$$V_\phi = 1e^{-6} \left(37.51 - 9.585e^{-2}\, T + 8.74e^{-4}\, T^2 - 5.044e^{-7}\, T^3\right) \tag{A7}$$

Reference pure-water densities in this study were at 8°C 999.85 kg/m^3 and at 20°C 998.21 kg/m^3.

Appendix B: Experimental Methods

B1. Sensor Compensation

Figure B1 shows the results of the sensor compensation explained in Section 2.1, CO_2 concentration plotted over overpressure.

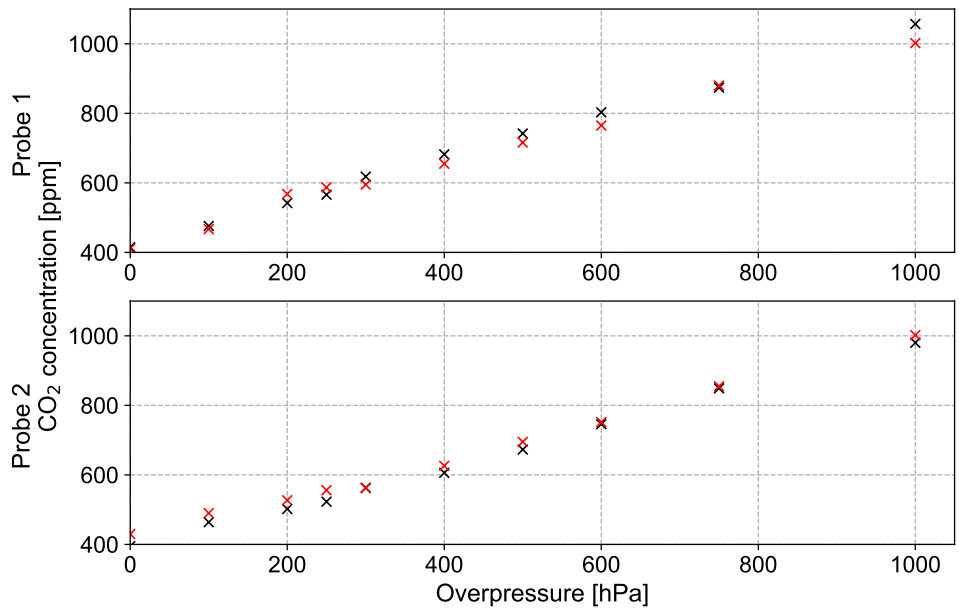

Figure B1. Compensation of the sensor probes, Probe 1 later installed at 1 m water depth and Probe 2 at 0.15 cm above ground.

Data Availability Statement

All implementations that were used for this study can be reproduced and found in a fixed version for download at https://git.iws.uni-stuttgart.de/dumux-pub/buerkle2021a. A tar-ball of the software is also part of the datasets, which are published in the Data Repository of the University of Stuttgart (DaRUS) (Class et al., 2021).

Acknowledgments
The work is associated (without receiving funding) with Project C04 of the Collaborative Research Center 1,313 (Project Number 327 154 368 – SFB 1313, German Research Foundation, DFG). The authors thank Harry Scherzer for providing inspiring ideas for this study. He is a geologist and a cave researcher and confronted us with his assumption of yet another mechanism with relevance for speleogenesis. The authors are grateful for very constructive comments from three anonymous reviewers, which helped us in shaping the presentation of our hypotheses, data, and results in this manuscript. Open Access funding enabled and organized by Projekt DEAL.

References

Atkinson, T. (1977). Carbon dioxide in the atmosphere of the unsaturated zone: An important control of groundwater hardness in limestones. *Journal of Hydrology*, *35*, 111–123. https://doi.org/10.1016/0022-1694(77)90080-4

Audra, P., & Palmer, A. (2011). The pattern of caves: Controls of epigenic speleogenesis. *Géomorphologie*, *17*(4), 359–378. https://doi.org/10.4000/geomorphologie.9571

Bakalowicz, M. (2005). Karst groundwater: A challenge for new resources. *Hydrogeology Journal*, *13*, 148–160. https://doi.org/10.1007/s10040-004-0402-9

Barrer, R., & Chio, H. (1965). Solution and diffusion of gases and vapours in silicone rubber membranes. *Journal of Polymer Science Part C: Polymer Symposia*, *10*, 111–138. https://doi.org/10.1002/polc.5070100111

Bell, R., Short, R., van Amerom, F., & Byrne, R. (2007). Calibration of an in situ membrane inlet mass spectrometer for measurements of dissolved gases and volatile organics in seawater. *Environmental Science & Technology*, *41*(23), 8123–8128. https://doi.org/10.1021/es070905d

Bénard, H. (1901). Les tourbillons cellulaires dans une nappe liquide. - Méthodes optiques d'observation et d'enregistrement. *Journal de Physique Théorique et Appliquée*, *10*(1), 254–266. https://doi.org/10.1051/jphystap:0190100100025400

Ben-Noah, I., & Friedman, S. (2018). Review and evaluation of root respiration and of natural and agricultural processes of soil aeration. *Vadose Zone Journal*, *17*, 170119. https://doi.org/10.2136/vzj2017.06.0119

Berean, K., Ou, J. Z., Nour, M., Latham, K., McSweeney, C., Paull, D., et al. (2014). The effect of crosslinking temperature on the permeability of pdms membranes: Evidence of extraordinary CO_2 and CH_4 gas permeation. *Separation and Purification Technology*, *122*, 96–104. https://doi.org/10.1016/j.seppur.2013.11.006

Bögli, A. (1980). *Karst hydrology and physical speleology*. Springer.

Bonacci, O. (1987). *Karst hydrology: With special reference to the Dinaric karst*. Springer.

Camilli, R., & Duryea, A. (2009). Characterizing spatial and temporal variability of dissolved gases in aquatic environments with in situ mass spectrometry. *Environmental Science & Technology*, *43*(13), 5014–5021. https://doi.org/10.1021/es803717d

Cioni, R., Guidi, M., Pierotti, L., & Scozzari, A. (2007). An automatic monitoring network installed in Tuscany (Italy) for studying possible geochemical precursory phenomena. *Natural Hazards and Earth System Sciences*, *7*, 405–416. https://doi.org/10.5194/nhess-7-405-2007

Class, H., Bürkle, P., Trötschler, O., Zimmer, M., & Strauch, B. (2021). *Data for: On the role of density-driven dissolution of CO_2 in karstification*. DaRUS. https://doi.org/10.18419/darus-2040

Class, H., Weishaupt, K., & Trötschler, O. (2020). Experimental and simulation study on validating a numerical model for CO_2 density-driven dissolution in water. *Water*, *12*, 738. https://doi.org/10.3390/w12030738

De Gregorio, S., Camarda, M., Longo, M., Cappuzzo, S., Giudice, G., & Gurrieri, S. (2011). Long-term continuous monitoring of the dissolved CO2 performed by using a new device in groundwater of the Mt. Etna (southern Italy). *Water Research*, *45*(9), 3005–3011. https://doi.org/10.1016/j.watres.2011.03.028

Dreybrodt, W. (1988). *Processes in karst systems - Physics, chemistry, and geology*. Springer.

Dreybrodt, W. (2004). Dissolution: Carbonate rocks. *Encyclopedia of Caves and Karst Science*, 295–298.

DuMux handbook. (2021). (Online accessed 1-July-2021). Retrieved from https://dumux.org/docs/handbook/master/dumux-handbook.pdf

Emami-Meybodi, H., Hassanzadeh, H., Green, C., & Ennis-King, J. (2015). Convective dissolution of CO_2 in saline aquifers: Progress in modeling and experiments. *International Journal of Greenhouse Gas Control*, *40*, 238–266. https://doi.org/10.1016/j.ijggc.2015.04.003

Ennis-King, J., & Paterson, L. (2003a). Rate of dissolution due to convective mixing in the underground storage of carbon dioxide. In J. Gale & Y. Kaya (Eds.), *Greenhouse gas control technologies* (Vol. 1, p. 507–510). Elsevier. https://doi.org/10.1016/b978-008044276-1/50081-7

Ennis-King, J., & Paterson, L. (2003b). Role of convective mixing in the long-term storage of carbon dioxide in deep saline formations. In *Annual fall technical conference and exhibition*, 5–8 October. Denver, CO. https://doi.org/10.2118/84344-ms

Erfani, H., Babaei, M., & Niasar, V. (2021). Dynamics of CO_2 density-driven flow in carbonate aquifers: Effects of dispersion and geochemistry. *Water Resources Research*, *57*, e2020WR027829. https://doi.org/10.1029/2020WR027829

Flekkøy, E. G., Oxaal, U., Feder, J., & Jøssang, T. (1995). Hydrodynamic dispersion at stagnation points: Simulations and experiments. *Physical Review E*, *52*(5), 4952–4962. https://doi.org/10.1103/physreve.52.4952

Fohlmeister, J., Voarintsoa, N., Lechnleitner, F., Boyd, M., Brandtstätter, S., Jacobson, M., & Oster, J. (2020). Main controls on the stable carbon isotope composition of speleothems. *Geochimica et Cosmochimica Acta*, *279*, 67–87. https://doi.org/10.1016/j.gca.2020.03.042

Ford, D., & Ewers, R. (1978). The development of limestone caves in the dimensions of length and depth. *International Journal of Speleology*, *10*, 213–244. https://doi.org/10.5038/1827-806x.10.3.1

Ford, D., & Williams, P. (2007). *Karst hydrogeology and geomorphology*. Wiley.

Gabrovšek, F., & Dreybrodt, W. (2000). Role of mixing corrosion in calcite-aggressive H_2O-CO_2-$CaCO_3$ solutions in the early evolution of karst aquifers in limestone. *Water Resources Research*, *36*, 1179–1188. https://doi.org/10.1029/1999WR900337

Garcia, J. (2001). *Density of aqueous solutions of CO_2 (Tech. Rep.). LBNL report 49023*, Lawrence Berkeley National Laboratory, Berkeley, CA, USA.

Green, C., & Ennis-King, J. (2018). Steady flux regime during convective mixing in three-dimensional heterogeneous porous media. *Fluids*, *3*(58), 1–21. https://doi.org/10.3390/fluids3030058

Gulley, J., Martin, J., & Moore, P. (2014). Vadose CO_2 gas drives dissolution at water tables in eogenetic karst aquifers more than mixing dissolution. *Earth Surface Processes and Landforms*, *39*, 1833–1846. https://doi.org/10.1002/esp.3571

Hage, E.-C. (2010). *Experimentelle Untersuchungen doppelt diffusiver Konvektion im Finger-Regime (Doctoral dissertation, Georg-August-Universität Göttingen)*. Retrieved from http://hdl.handle.net/11858/00-1735-0000-0006-B4CD-D

Hassanzadeh, H., Pooladi-Darvish, M., & Keith, D. (2005). Modelling of convective mixing in CO_2 storage. *Journal of Canadian Petroleum Technology*, *44*(10). https://doi.org/10.2118/05-10-04

Hassanzadeh, H., Pooladi-Darvish, M., & Keith, D. (2006). Stability of a fluid in a horizontal saturated porous layer: Effect of non-linear concentration profile, initial, and boundary conditions. *Transport in Porous Media*, *65*(2), 193–211. https://doi.org/10.1007/s11242-005-6088-1

Hassanzadeh, H., Pooladi-Darvish, M., & Keith, D. (2007). Scaling behavior of convective mixing, with application to geological storage of CO_2. *American Institute of Chemical Engineers Journal*, *53*, 1121–1131. https://doi.org/10.1002/aic.11157

Houillon, N., Lastennet, R., Denis, A., & Malaurent, P. (2020). The CO_2 dynamics in the continuum atmosphere-soil-epikarst and its impact on the karstification potential of water: A case study of the lasceaux cave site (Montignac, France). In C. Bertrand, S. Denimal, M. Steinmann, & P. Renard (Eds.), *Eurokarst 2018, Besancon - Advances in the Hydrogeology of Karst and Carbonate Reservoirs* (p. 93–99). Springer Nature Switzerland. https://doi.org/10.1007/978-3-030-14015-1_11

IPCC. (2005). Special report on carbon dioxide capture and storage (Tech. Rep.). Cambridge University Press, Cambridge, United Kingdom and New York, NY, USA: *Intergovernmental Panel on Climate Change (IPCC), prepared by Working Group III*. In B.Metz, O. Davidson, H. C. de Conink, M. Loos and L. A. Meyer (Eds). Retrieved from https://www.ipcc.ch/site/assets/uploads/2018/03/srccs_wholereport-1.pdf

Javaid, A. (2005). Membranes for solubility-based gas separation applications. *Chemical Engineering Journal*, *112*(1–3), 219–226. https://doi.org/10.1016/j.cej.2005.07.010

Johnson, M., Billett, M., Dinsmore, K., Wallin, M., Dyson, K., & Jassal, R. (2010). Direct and continuous measurement of dissolved carbon dioxide in freshwater aquatic systems method and applications. *Ecohydrology*, *3*(1), 68–78. https://doi.org/10.1002/eco.95

Kana, T., Darkangelo, C., Hunt, M., Oldham, J., Bennett, G., & Cornwell, J. (1994). Membrane inlet mass spectrometer for rapid high-precision determination of N_2, O_2, and Ar in environmental water samples. *Analytical Chemistry*, *66*(23), 4166–4170. https://doi.org/10.1021/ac00095a009

Kaufmann, G., Gabrovšek, F., & Romanov, D. (2014). Deep conduit flow in karst aquifers revisited. *Water Resources Research*, *50*, 4821–4836. https://doi.org/10.1002/2014WR015314

Kellner, M. (2016). *Experimentelle Untersuchungen von Fingerströmung und thermohalinen Treppen für instabile Auftriebsverhältnisse (Doctoral dissertation, Georg-August-Universität Göttingen)*. Retrieved from http://hdl.handle.net/11858/00-1735-0000-0028-8732-4

Kjeldsen, P. (1993). Evaluation of gas diffusion through plastic materials used in experimental and sampling equipment. *Water Research*, *27*(1), 121–131. https://doi.org/10.1016/0043-1354(93)90202-S

Klimchouk, A., Ford, D., Palmer, A., & Dreybrodt, W. (Eds.). (2000). *Speleogenesis - Evolution of Karst Aquifers*. National Speleological Society.

Koch, T., Gläser, D., Weishaupt, K., Ackermann, S., Beck, M., Becker, B., et al. (2020). DuMu^x 3 – An open-source simulator for solving flow and transport problems in porous media with a focus on model coupling. *Computers & Mathematics with Applications*. https://doi.org/10.1016/j.camwa.2020.02.012

Kukuljan, L., Gabrovšek, F., Covington, M., & Johnston, V. (2021). CO2 dynamics and heterogeneity in a cave atmosphere: Role of ventilation patterns and airflow pathways. *Theoretical and Applied Climatology*, *146*, 91–109. https://doi.org/10.1007/s00704-021-03722-w

Lai, F., & Kulacki, F. (1990). The influence of lateral mass flux on mixed convection over inclined surfaces in saturated porous media. *Journal of Heat Transfer*, *112*(2), 515–518. https://doi.org/10.1115/1.2910414

Lai, F., & Kulacki, F. (1991). Experimental study of free and mixed convection in horizontal porous layers locally heated from below. *International Journal of Heat and Mass Transfer*, *34*(2), 525–541. https://doi.org/10.1016/0017-9310(91)90271-F

Lee, K. Y., van Geldern, R., & Bart, J. A. (2021). Extreme gradients in CO_2 losses downstream of karstic springs. *The Science of the Total Environment*, *778*, 146099. https://doi.org/10.1016/j.scitotenv.2021.146099

Lindeberg, E., & Wessel-Berg, D. (1997). Reservoir storage and containment of greenhouse gases. *Transport in Porous Media*, *38*, S229–S234. https://doi.org/10.1016/s0196-8904(96)00274-9

Lord Rayleigh, O. F. (1916). Lix. on convection currents in a horizontal layer of fluid, when the higher temperature is on the under side. *The London, Edinburgh, and Dublin Philosophical Magazine and Journal of Science*, *32*(192), 529–546. https://doi.org/10.1080/14786441608635602

Ma, J., Lio, R., Tsang, L.-S., Lan, Z.-D., & Li, Y. (2014). A downward CO_2 flux seems to have nowhere to go. *Biogeosciences*, *11*, 6251–6262. https://doi.org/10.5194/bg-11-6251-2014

Mangin, A. (1975). *Contribution à l'étude hydrodynamique des aquifères karstiques (Doctoral dissertation, Université de Dijon, Sciences de la Terre)*. Retrieved from https://hal.archives-ouvertes.fr/tel-01575806

Merkel, T., Bondar, V., Nagai, K., Freeman, B., & Pinnau, I. (2000). Gas sorption, diffusion, and permeation in poly(dimethylsiloxane). *Journal of Polymer Science: Part B: Polymer Physics*, *38*, 415–434. https://doi.org/10.1002/(sici)1099-0488(20000201)38:3<415::AID-POLB8>3.0.CO;2-Z

Michel-Meyer, I., Shavit, U., Tsinober, A., & Rosenzweig, R. (2020). The role of water flow and dispersive fluxes in the dissolution of CO_2 in deep saline aquifers . *Water Resources Research*, *56*(11), e2020WR028184. https://doi.org/10.1029/2020WR028184

Mohammadi, Z., Raeisi, E., & Bakalowicz, M. (2007). Method of leakage study at the karst dam site. A case study: Khersan 3 Dam, Iran. *Environmental Geology*, *52*, 1053–1065. https://doi.org/10.1007/s00254-006-0545-1

Pau, G., Bell, J., Pruess, K., Almgren, A., Lijewski, M., & Zhang, K. (2010). High resolution simulation and characterization of density-driven flow in CO_2 storage in saline aquifers. *Advances in Water Resources*, *33*, 443–455. https://doi.org/10.1016/j.advwatres.2010.01.009

Peyraube, N., Lastennet, R., Denis, A., Malaurent, P., & Villanueva, J. (2015). Interpreting CO_2-SIc relationship to estimate CO_2 baseline in limestone aquifers. *Environmental Earth Sciences*, *1*, 19–26. https://doi.org/10.1007/s12665-014-3316-4

Pinnau, I., & He, Z. (2004). Pure and mixed gas permeation properties of polydimethylsiloxane for hydrocarbon/methane and hydrocarbon/hydrogen separation. *Journal of Membrane Science*, *244*(1–2), 227–233. https://doi.org/10.1016/j.memsci.2004.06.055

Raharjo, R., Freemann, B., Paul, D., Sarti, G., & Sanders, E. (2007). Pure and mixed gas CH_4 and n-C_4H_{10} permeability and diffusivity in poly(dimethylsiloxane). *Journal of Membrane Science*, *306*(1–2), 75–92. https://doi.org/10.1016/j.memsci.2007.08.014

Riaz, A., Hesse, M., Tchelepi, H., & Orr, F. (2006). Onset of convection in a gravitationally unstable diffusive boundary layer in porous media. *Journal of Fluid Mechanics*, *548*, 87–111. https://doi.org/10.1017/S0022112005007494

Riechelmann, S., Breitenbach, S., Schröder-Ritzrau, A., Mangini, A., & Immenhauser, A. (2019). Ventilation and cave air PCO_2 in the Bunker-Emst Cave System (NW Germany): Implications for speleothem proxy data. *Journal of Cave and Karst Studies*, *81*(2), 98–112. https://doi.org/10.4311/2018ES0110

Scholes, C., Kentish, S., & Stevens, G. (2009). The effect of condensable minor components on the gas separation performance of polymeric membranes for carbon dioxide capture. *Energy Procedia*, *1*, 311–317. https://doi.org/10.1016/j.egypro.2009.01.043

Schultz, J., & Peinemann, K. (1996). Membranes for separation of higher hydrocarbons from methane. *Journal of Membrane Science*, *110*(1), 37–45. https://doi.org/10.1016/0376-7388(95)00214-6

Serrano-Ortiz, P., Roland, M., Sanchez-Moral, S., Janssens, I., Domingo, F., Goddéris, Y., & Kowalsko, A. (2010). Hidden, abiotic CO_2 flows and gaseous reservoirs in the terrestrial carbon cycle: Review and perspectives. *Agricultural and Forest Meteorology*, *150*, 321–329. https://doi.org/10.1016/j.agrformet.2010.01.002

Spötl, C., Desch, A., Dublyansky, Y., Plan, L., & Mangini, A. (2016). Hypogene speleogenesis in dolimite host rock by CO_2-rich fluids, Kozak Cave (southern Austria). *Geomorphology*, *255*, 39–48. https://doi.org/10.1016/j.geomorph.2015.12.001

Stern, S., Shah, V., & Hardy, B. (1987). Structure-permeability relationships in silicone Polymers. *Journal of Polymer Science: Part B: Polymer Physics*, *25*, 1263–1298. https://doi.org/10.1002/polb.1987.090250607

Stevanovic, Z. (2015). *Karst aquifers - Characterization and Engineering*. Springer.

Strauch, B., Heeschen, K. U., Schicks, J. M., Spangenberg, E., & Zimmer, M. (2020). Application of tubular silicone (PDMS) membranes for gas monitoring in CO_2–CH_4 hydrate exchange experiments. *Marine and Petroleum Geology*, *122*, 104677. https://doi.org/10.1016/j.marpetgeo.2020.104677

Weir, G. J., White, S. P., & Kissling, W. M. (1996). Vertical convection in an aquifer column under a gas cap of CO_2. *Energy Conversion and Management*, *23*, 37–60. https://doi.org/10.1007/BF00145265

Werth, M., & Kuzyakov, Y. (2010). 13C fractionation at the root-microorganisms-soil interface: A review and outlook for partitioning studies. *Soil Biology and Biochemistry*, *43*(9), 1372–1384. https://doi.org/10.1016/j.soilbio.2010.04.009

White, W. (2018). *Caves and karst of the Greenbrier valley in West Virginia*. Springer.

Zimmer, M., Erzinger, J., Kujawa, C., & CO2-SINK-Group. (2011). The gas membrane sensor (GMS): A new method for gas measurements in deep boreholes applied at the CO_2 SINK site. *International Journal of Greenhouse Gas Control*, *5*, 995–1001. https://doi.org/10.1016/j.ijggc.2010.11.007